

Suppression of magnetic ordering in XXZ-type antiferromagnetic monolayer NiPS₃

*Kangwon Kim,[†] Soo Yeon Lim,[†] Jae-Ung Lee,[†] Sungmin Lee,^{‡,§} Tae Yun Kim,^{§,¶} Kisoo Park,^{‡,§}
Gun Sang Jeon,[#] Cheol-Hwan Park,^{§,¶,*} Je-Geun Park,^{‡,§,*} and Hyeonsik Cheong^{†,*}*

[†]Department of Physics, Sogang University, Seoul 04107, Korea

[‡]Center for Correlated Electron Systems, Institute for Basic Science, Seoul 08826, Korea

[§]Department of Physics and Astronomy, Seoul National University, Seoul 08826, Korea

[¶]Center for Theoretical Physics, Seoul National University, Seoul 08826, Korea

[#]Department of Physics, Ewha Womans University, Seoul 03760, Korea

Correspondence and requests for materials should be addressed to C.-H.P. (email:

cheolhwan@snu.ac.kr), J.-G.P (email: jgpark10@snu.ac.kr), or H.C. (email:

hcheong@sogang.ac.kr)

ABSTRACT

How a certain ground state of complex physical systems emerges, especially in two-dimensional materials, is a fundamental question in condensed-matter physics. A particularly interesting case is systems belonging to the class of XY Hamiltonian where the magnetic order parameter of conventional nature is unstable in two-dimensional materials leading to a Berezinskii-Kosterlitz-Thouless transition. Here, we report how the XXZ-type antiferromagnetic order of a magnetic van

der Waals material, NiPS₃, behaves upon reducing the thickness and ultimately becomes unstable in the monolayer limit. Our experimental data are consistent with the findings based on renormalization group theory that at low temperatures a two-dimensional XXZ system behaves like a two-dimensional XY one, which cannot have a long-range order at finite temperatures. This work provides experimental examination of the XY magnetism in the atomically thin limit and opens new opportunities of exploiting these fundamental theorems of magnetism using magnetic van der Waals materials.

KEYWORDS: Two-dimensional magnetism, Antiferromagnetism, XXZ/XY Hamiltonian, Monolayer NiPS₃, Raman spectroscopy

It is an enduring theme of physical science how a certain ground state emerges out of often complex underlying principles of nature. Our understanding of this fundamental question captures all the essence of what we know about the system, be it cosmos or real materials. One prime example is magnetism in two-dimensional (2D) systems. Unlike in one- or three- dimension, fluctuations are sensitive to the symmetry of the order parameters; Ising, XY, and Heisenberg types. Of the three types, the Ising Hamiltonian was the first to be solved by Onsager¹. About twenty years later, there were theoretical breakthroughs for the Heisenberg model²⁻⁴.

For the XY model, the trio of Berezinskii⁵ and Kosterlitz and Thouless⁶ demonstrated independently that the 2D XY system hosts a very unusual ground state of an algebraic order at low temperatures through what is now known as the Berezinskii-Kosterlitz-Thouless (BKT) transition. The generic form of the magnetic Hamiltonian can be written as follows⁷:

$$H = -\sum_{\langle i,j \rangle} (J_x S_i^x S_j^x + J_y S_i^y S_j^y + J_z S_i^z S_j^z), \quad (1)$$

where $J_{x,y,z}$ is the nearest-neighbor exchange interaction for spin components, and i and j run through all lattice sites and nearest neighbors, respectively. S_i^x , S_i^y , and S_i^z are the x , y , and z component of the total spin at i -site. The critical behaviors of two-dimensional magnetic systems have been studied using layered magnetic crystals or ultra-thin metal films⁸. However, it is still desirable for one to investigate the major features of 2D magnetism using true 2D material. For the 2D Ising system ($J_x = J_y = 0$) the magnetic ground state is stable even in the 2D limit, whose experimental evidence has been recently presented using magnetic van der Waals materials: FePS₃^{9,10} with antiferromagnetic order and Cr₂Ge₂Te₆¹¹ and CrI₃¹² with ferromagnetic order.

With the success in the recent experimental investigation of 2D Ising systems, one can think of using these newly found magnetic van der Waal materials for the studies of the XY model

($J_x = J_y$, $J_z = 0$), which is far more interesting and expected to host much richer physics. One can generalize the problems for two dimensions by using the XXZ model ($J_x = J_y \neq J_z$). We note that from renormalization-group studies^{13,14}, an antiferromagnetic 2D quantum-spin system with easy-plane-like anisotropy, no matter how small the anisotropy is, behaves like an XY system at low temperatures. With the advent of a new class of magnetic van der Waals materials, one at last seems to have the right materials to start with^{15,16}.

Transition metal phosphorus trisulfides (TMPS₃, TM = V, Mn, Fe, Co, Ni, or Zn) are a new class of antiferromagnetic van der Waals materials that are suitable for studying antiferromagnetic ordering in the 2D limit: FePS₃ of Ising-type, NiPS₃ of XY or XXZ-type, and MnPS₃ of Heisenberg-type^{17,18}. They can be easily exfoliated into few atomic layers¹⁹, allowing one to examine the dependence of the magnetic ordering on the dimensionality. There still remains one experimental difficulty: since antiferromagnets do not have a finite net magnetization, detection of antiferromagnetic ordering in few-layer samples, let alone monolayer, is extremely challenging¹⁵.

Raman spectroscopy has proven to be a powerful technique for the studies of 2D materials. Since the Raman spectrum changes sensitively with the thickness^{20,21}, it is suitable not only to determine structural parameters such as the number of layers but also to study thickness-dependent physical properties. In particular, it is possible to study magnetic properties by exploiting the spin dependence of Raman processes. For example, two-magnon Raman scattering is often used to study antiferromagnetism^{22,23}, and Raman spectroscopy has been successfully used to investigate the Ising-type antiferromagnet FePS₃^{9,10}. By monitoring the appearance of a series of new Raman modes due to doubling of the unit cell upon antiferromagnetic ordering, it was found that the Ising-type magnetic order of FePS₃ is preserved down to the monolayer limit. In this work, we measured

the Raman signatures of the antiferromagnetic ordering in NiPS₃ as a function of the number of layers down to monolayer, and found that the ordering persists down to 2 layers (2L) but is dramatically suppressed in the monolayer (1L) limit. At the same time, there is persistent spin fluctuations even in monolayer samples. These experimental findings from monolayer systems are consistent with the theoretical predictions of the XY model^{5,6}.

Results

Crystal and magnetic structures of NiPS₃. Bulk NiPS₃ has a monoclinic structure with the point group C_{2h} , whereas monolayer NiPS₃ has a hexagonal structure with the point group D_{3d} ^{19,24,25}. As shown in Fig. 1a, Ni atoms are arranged in a hexagonal lattice, each of them being surrounded by six S atoms with trigonal symmetry. These S atoms are connected to two P atoms located above and below the Ni plane. Two P atoms and six S atoms are covalently bonded among themselves, forming a (P₂S₆)⁴⁻ anion complex of a pyramidal structure. The layers are weakly bound to each other by van der Waals interaction along the *c*-axis and can be easily exfoliated to atomically thin few-layer samples¹⁹. Figure 1b is an atomic force microscope image of one of the exfoliated monolayer NiPS₃ samples measured in this work (see Supplementary Fig. 1 for samples with other thicknesses).

Recent neutron diffraction studies have shown that below Néel temperature (T_N) spins in bulk NiPS₃ are aligned mostly in the *ab* plane with a small component along the *c*-axis^{17,18}, which is consistent with the temperature dependence of the magnetic susceptibility (see Supplementary Fig. 2). The ordered magnetic moments appear to point more towards the *a*-axis than the *b*-axis and the same-spin chains are aligned along the zigzag direction^{17,18} as shown by the red arrows in Fig. 1a. We note that due to the *ab* anisotropy, this is not an exact XXZ system, but an approximate one.

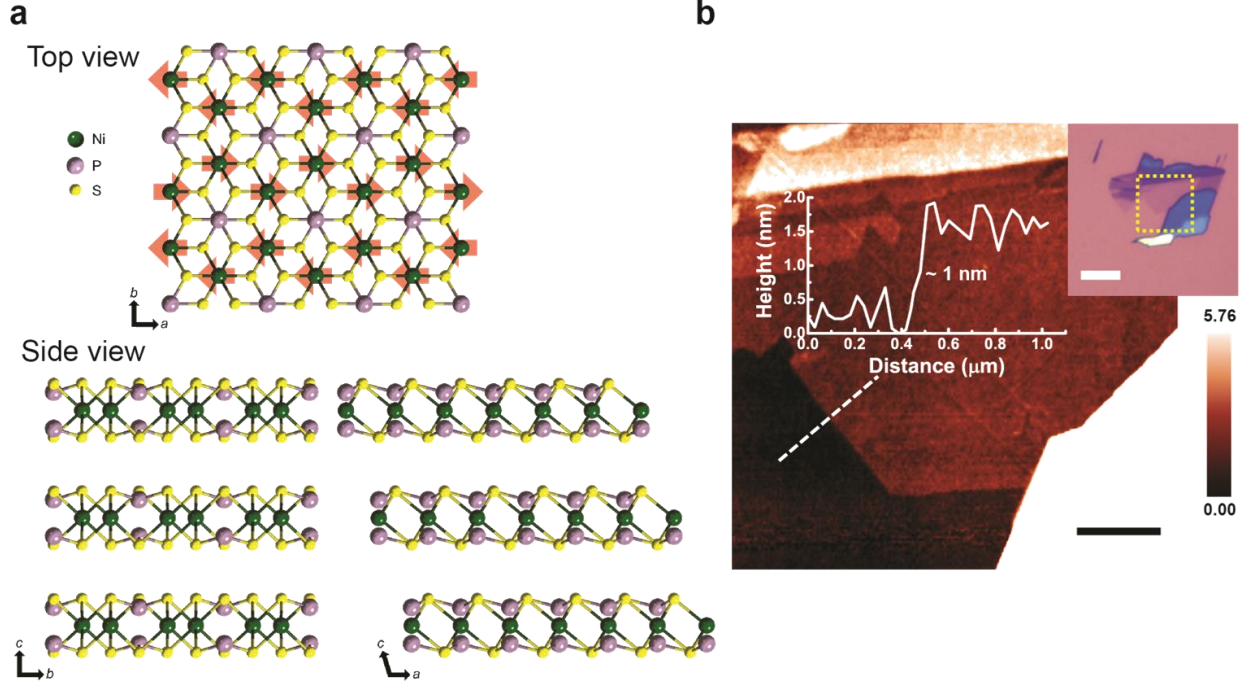


Fig. 1 Magnetic van der Waals material NiPS₃. **a**, Crystal structure of NiPS₃. Red arrows indicate the spin orientations of Ni atoms below Néel temperature (T_N). **b**, Atomic force microscope image and thickness line profile of monolayer NiPS₃. Optical image of the sample is shown in inset. The black and white scale bars are 1 and 5 μm , respectively.

Raman signatures of the antiferromagnetic phase transition. Figure 2 compares polarized Raman spectra of bulk NiPS₃ in two different phases: antiferromagnetic phase at $T=10$ K and paramagnetic phase at $T=295$ K. All the peaks in the Raman spectra are labelled as $P_1, P_2, \text{etc.}$ in the order of increasing frequency. As bulk paramagnetic NiPS₃ belongs to the C_{2h} point group²⁵, the zone center phonon modes are represented by $\Gamma = 8A_g + 7B_g + 6A_u + 9B_u$. In the backscattering geometry, both the A_g and B_g modes are Raman allowed in the parallel-polarization scattering configuration $[\bar{z}(xx)z]$ whereas only the B_g modes are active in the cross-polarization scattering configuration $[\bar{z}(xy)z]$. The Raman modes at higher frequencies are mostly attributed to the intramolecular vibrations from $(\text{P}_2\text{S}_6)^{4-}$ bipyramid structures: similar features were previously observed

for FePS_3 ⁹. On the other hand, the low-frequency peaks (P_1 and P_2) are due to vibrations involving the heavy Ni atoms²⁵.

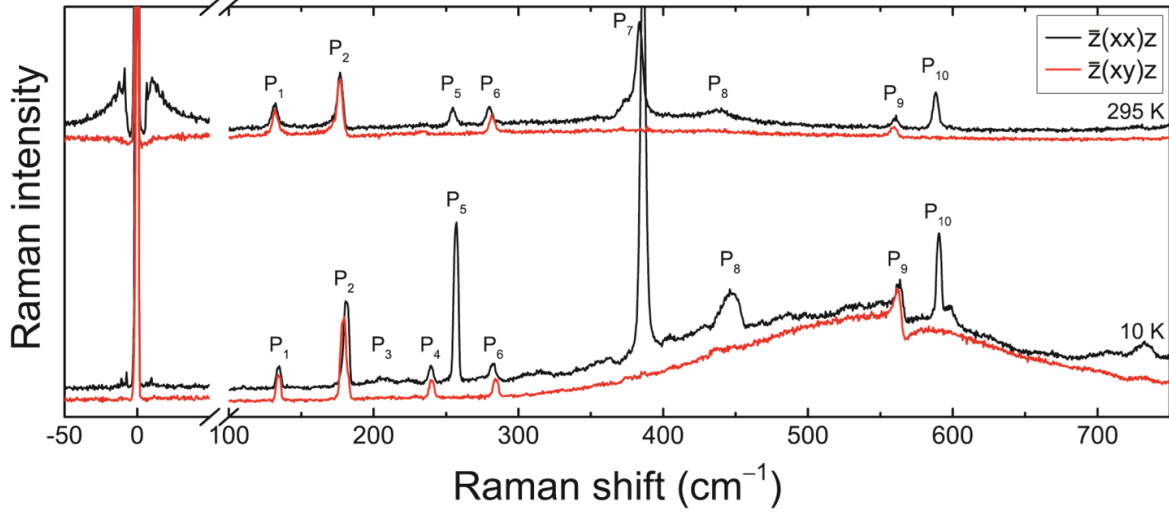


Fig. 2 Raman spectra of bulk NiPS_3 . Comparison of Raman spectra measured at $T=10$ and 295 K in parallel $[\bar{z}(xx)z]$ (black) and cross $[\bar{z}(xy)z]$ (red) polarization scattering configurations.

The most prominent difference between paramagnetic ($T=295$ K) and antiferromagnetic ($T=10$ K) phases is the appearance of the broad peak centered at ~ 550 cm^{-1} in the antiferromagnetic phase due to two-magnon scattering, or the double spin-flip processes via the exchange mechanism in antiferromagnets with the collinear structure^{22,26}. The spin orientation of Ni atoms lies largely on the ab plane with some c -axis component due to the magnetic ordering at low temperature, and the two-magnon signals become well defined. We note that the two-magnon Raman signals are consistent with our calculations of the two-magnon spectrum using the XXZ Hamiltonian (see Supplementary Note 1 and Supplementary Fig. 3). Also, the clear signals centered at 0 cm^{-1} in the spectrum obtained in the parallel-polarization configuration at $T=295$ K are ascribed to quasi-elastic scattering (QES) from magnetic fluctuations, which is often observed in low-dimensional spin systems^{23,27,28}. These QES signals become considerably weakened at lower temperatures since

the spin fluctuations are suppressed in the magnetically ordered phase. Unlike the two-magnon signal which does not depend on the polarization, the QES signal is much stronger in parallel polarization, presumably because low-energy spin fluctuations do not change the polarization of the scattered photon very much. In addition, the peak P₉ shows a prominent Breit-Wigner-Fano (BWF) line shape due to Fano resonance at low temperatures²⁹. Fano resonance requires quantum interference between a discrete excitation and a continuum³⁰ and the BWF line shape is described by^{30,31}:

$$I(\omega) = I_0 \frac{[1 + 2(\omega - \omega_0) / (q\Gamma)]^2}{[1 + 4(\omega - \omega_0)^2 / \Gamma^2]}, \quad (2)$$

where ω_0 is the bare phonon frequency, Γ the linewidth, and q the asymmetry parameter, where $|1/q|$ correlates with the strength of the coupling. In this case, the discrete excitation is the emission of a phonon, whereas the continuum corresponds to the broad two-magnon excitation. We note that P₉ is the only peak that appears in the Raman spectra obtained in the cross-polarization configuration among the peaks that have significant overlap with the two-magnon continuum.

According to our calculations (See Supplementary Table 1 and Supplementary Fig. 4), the phonon modes associated with the P₉ peak are two almost-degenerate E_g -like modes. Thanks to the in-plane E_g -like nature of these modes, they appear in both parallel- and cross-polarization Raman scattering configurations. Our Raman data show that in the energy range where the two-magnon continuum is strong, only these E_g -like modes couple strongly to the two-magnon continuum at low temperatures. This finding is indeed in good agreement with Rosenblum *et al*²⁹. Similar strong phonon-magnon coupling for in-plane phonons was also observed in (Y,Lu)MnO₃, a model compound for spins on a 2D triangular lattice³². We note that although P₅ and P₇ show

strong relative enhancement at low temperatures, their peak positions or intensities do not show any correlation with magnetic ordering (see Supplementary Fig. 5).

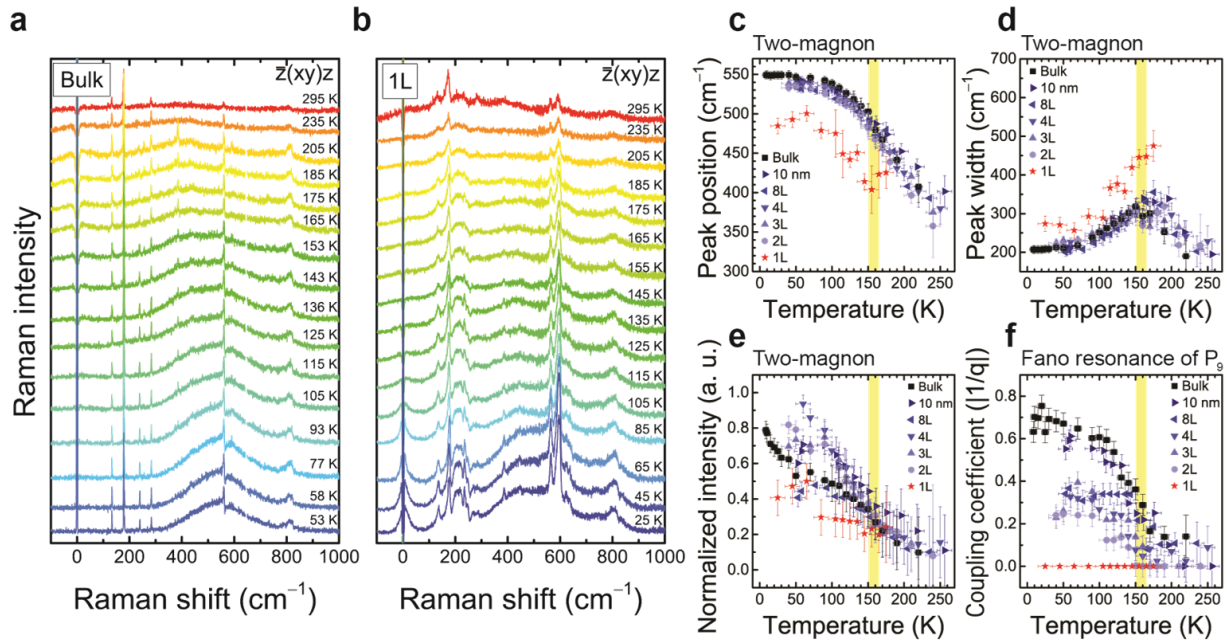


Fig. 3 Temperature dependence of two-magnon signals and Fano resonance of P_9 . **a,b**, Raman spectra of bulk (**a**) and monolayer (**b**) NiPS_3 in cross polarization as a function of temperature. **c–f**, Peak position (**c**), width (**d**), and normalized intensity (**e**) of two-magnon signals; and coupling coefficient ($|1/q|$) of Fano resonance of P_9 (**f**) as a function of temperature for various thicknesses. Error bars indicate the experimental uncertainties in temperature and the uncertainties in the fitting procedure to determine each parameter.

Two-magnon scattering and Fano resonance of NiPS_3 . In order to study the thickness dependence of the antiferromagnetic ordering, we measured the temperature dependence of the Raman spectra as a function of the number of layers down to the monolayer limit. Figure 3a shows the temperature dependence of the Raman spectrum of bulk NiPS_3 measured in the cross-polarization configuration. Suppression of several phonon peaks makes it easier to monitor the two-magnon signals in the cross-polarization configuration. In these data, we observe that the two-magnon signals gradually grow and shift towards higher frequencies as the temperature decreases

below T_N . These observations are typical of antiferromagnetic materials, where the two-magnon signals redshift and become broader and weaker as the spectral weight is shifted to quasi-elastic scattering when the temperature is increased^{27,28,33,34}. We have carried out similar measurements for few-layer samples with different thicknesses (see Supplementary Fig. 6) and the results are summarized in Figs. 3c-f. The peak position, intensity, and width of the two-magnon signals show little dependence on the number of layers from bulk all the way down to 2 layers. The coupling strength of Fano resonance, represented by $|1/q|$, also shows dramatic enhancement below bulk T_N . On the other hand, the spectrum of monolayer NiPS₃ seems to have a qualitatively different temperature dependence from that of samples with other thicknesses. For example, Fig. 3b shows the temperature dependence of the Raman spectrum of monolayer NiPS₃ as a function of temperature. Unlike other samples thicker than monolayer, the two-magnon feature is not well defined even when the temperature is much lower than the bulk T_N . The position of the two-magnon peak is also considerably lower in frequency than in the case of thicker samples. Furthermore, the peak P₉ does not show any indication of Fano resonance. All these observations point to the conclusion that antiferromagnetic ordering is not fully developed in monolayer NiPS₃ even at the lowest temperature measured (25 K).

Magnetic-order-induced frequency difference for P₂ phonons. Interestingly enough, a closer inspection of the bulk spectra in Fig. 2 reveals that P₂ comprises two peaks at low temperatures as the peak position is slightly different under different polarization configurations. The higher frequency peak (P₂^{||}) appears in the parallel-polarization configuration, while the lower frequency peak (P₂[⊥]) is seen in the cross-polarization configuration (see Supplementary Fig. 7 for complete polarization dependence data). We should emphasize that there is minimal difference in the phonon frequency in the data taken at $T=295$ K. Figure 4a shows the temperature dependence of

the polarized Raman spectra of bulk NiPS₃ in the range 120–300 cm⁻¹. We can see a clear sign of the temperature-dependent phonon frequency difference for P₂. On the other hand, P₆ also shows a small peak frequency difference in two polarization configurations, which does not seem to depend much on the temperature (see Fig. 4b for the summary). If we compare the phonon frequency difference of P₂ with the susceptibility data (Fig. 4c), the cross correlation between them is evident.

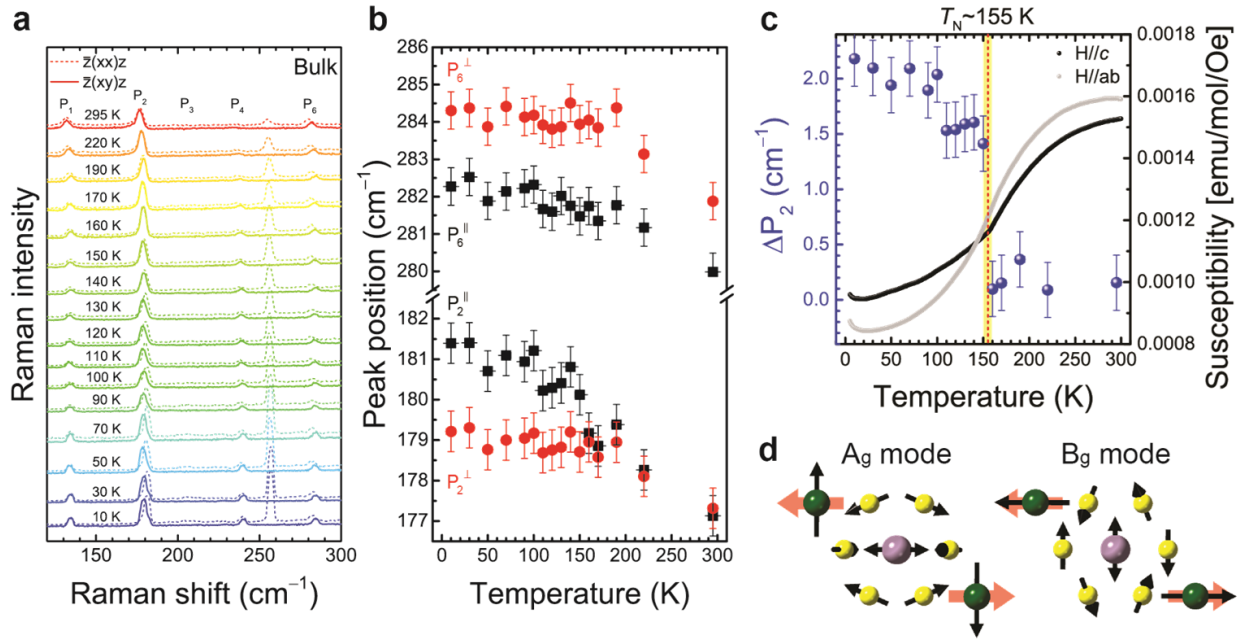


Fig. 4 Magnetic-order-induced frequency difference for phonon P₂. **a**, Polarized Raman spectra of bulk NiPS₃ as a function of the temperature. **b**, Peak positions of P₂ and P₆ obtained in parallel (black squares, P₂^{||} and P₆^{||}) and cross (red circles, P₂[⊥] and P₆[⊥]) polarization configurations as a function of the temperature. **c**, Temperature dependences of phonon frequency difference ΔP_2 ($\Delta P_2 \equiv |P_2^{\parallel} - P_2^{\perp}|$, blue circles) and susceptibility of bulk NiPS₃. The error bars indicate experimental uncertainties. **d**, Schematics of lattice-vibration patterns associated with A_g and B_g modes near ~180 cm⁻¹. Black arrows indicate the direction of atomic displacement and thick red arrows indicate spin orientations of Ni atoms below T_N.

In order to elucidate the origin of this phonon frequency difference, theoretical calculations of the vibrational modes in the ordered phase were carried out using density functional theory (DFT)

with the frozen phonon method. It was found that near the frequency of P_2 , there are two phonon modes with similar frequencies but with different symmetries. These modes originate from the doubly degenerate E -like modes of monolayer NiPS_3 , which are split due to monoclinic stacking of the layers. However, due to the weak interlayer coupling, this splitting is expected to be very small in the paramagnetic phase²⁵. Experimentally, we observed almost zero separation between the two peaks measured in the parallel- and cross-polarization configurations in the paramagnetic phase. We further note that we did not observe any superlattice peaks from our single crystal X-ray diffraction experiments performed at temperatures as low as 20 K. Therefore, we can conclude that the temperature dependence of the splitting of P_2 arising from structural symmetry breaking should be very small, if at all. Figure 4d illustrates these two vibrational modes in the antiferromagnetic phase. The A_g mode involves vibrations of the Ni atoms in the periodic direction of the same-spin zigzag chains (see Fig. 1a), whereas the B_g mode involves Ni atoms vibrating parallel to this direction. Owing to the relative directions of the vibration and the distribution of the spin polarization, the vibrational frequencies shift differently upon antiferromagnetic ordering and results in observed increase in the phonon frequency difference ΔP_2 , which is mostly of magnetic origin. Since the other peaks do not show any dramatic changes with temperature, one can also exclude a structural phase transition as the origin of this phonon frequency difference. We note that a similar phonon frequency difference below critical temperature³⁵ has been reported for $\text{Cr}_2\text{Ge}_2\text{Te}_6$.

We note that in the spectra for thinner samples there are several peaks that originate from multi-phonon scattering at ~ 210 , ~ 590 , and $\sim 800 \text{ cm}^{-1}$ (see Supplementary Fig. 8). Some of these peaks are strongly enhanced due to the resonance effect. Similar enhancement effects on multi-phonon peaks due to resonance have been observed in other 2D materials³⁶⁻³⁸. For example, the

relative intensities or the line shapes of P_3 at $\sim 210 \text{ cm}^{-1}$ or the peak at $\sim 590 \text{ cm}^{-1}$ vary with the excitation laser energy, which is a clear indication of resonant processes (see Supplementary Note 2 and Supplementary Fig. 9). We further checked the temperature dependence of P_3 for 1-4L NiPS₃ (see Supplementary Fig. 10). Since the frequency and the intensity of P_3 does not exhibit any significant change near the Néel temperature, we can safely conclude that P_3 is not related to the magnetic ordering.

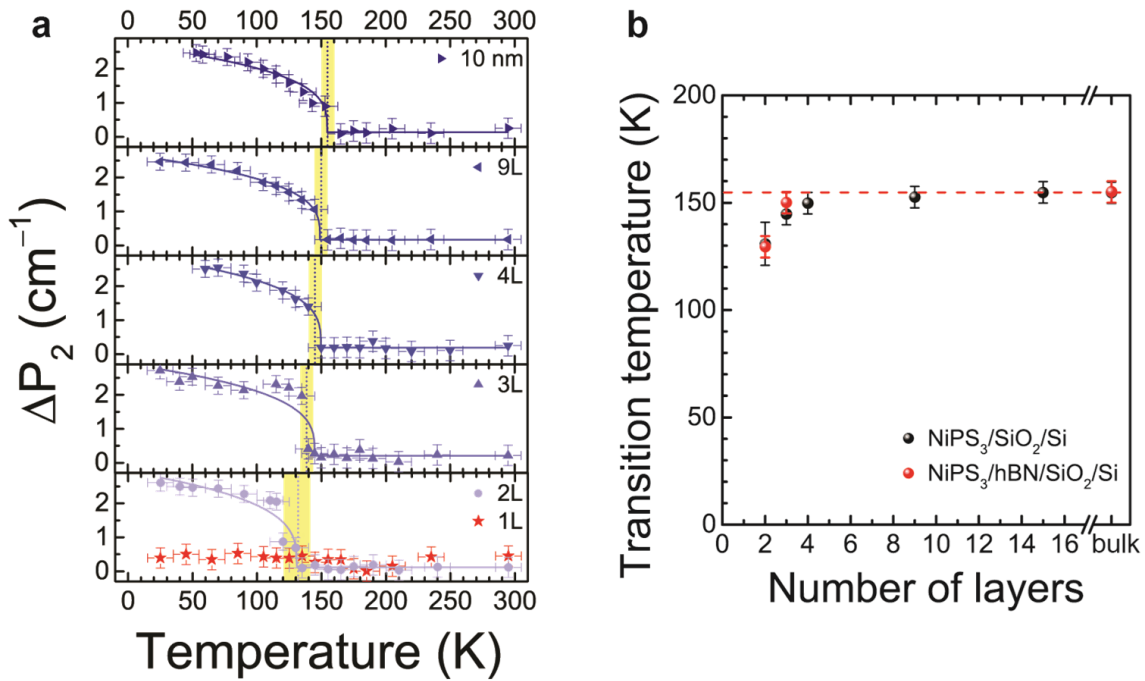


Fig. 5 Thickness dependence of Néel temperature for few-layer NiPS₃. **a**, Temperature dependence of magnetic-order-induced frequency difference ΔP_2 for various thicknesses. The error bars indicate experimental uncertainties, the dashed vertical lines indicate the Néel temperature for each thickness, and the solid curves are fitting results by using the spin-induced phonon frequency shift model. **b**, Estimated antiferromagnetic transition temperature for various thicknesses by using ΔP_2 of NiPS₃ samples on SiO₂/Si (black) and hBN/SiO₂/Si (red) substrates. The error bars indicate experimental uncertainties, and the red dashed line shows bulk Néel temperature (155 K).

Estimation of Néel temperature of few-layer NiPS₃ from ΔP_2 . Now, we would like to inspect this frequency difference as a function of temperature for few-layer NiPS₃ (see Supplementary Fig. 11). Figure 5a shows temperature dependence of ΔP_2 for various thicknesses including monolayer. The antiferromagnetic transition temperatures are extracted by using the spin-induced phonon frequency shift model^{39,40} (see Supplementary Note 3 and Supplementary Fig. 12 for details) and summarized in Fig. 5b. As seen in Fig. 5a, ΔP_2 shows a clear onset for 2-layer or thicker samples and the transition temperature gets slightly lower as the thickness decreases. On the contrary, ΔP_2 for monolayer NiPS₃, if any, is virtually temperature independent. These results confirm our conclusion from the analysis of the two-magnon signals: (1) the antiferromagnetic transition temperature (T_N) depends only slightly on the thickness for 2-layer or thicker NiPS₃, and (2) antiferromagnetic ordering is significantly suppressed in monolayer NiPS₃.

In order to rule out the possible extrinsic effect due to the substrate, we fabricated additional samples on hexagonal boron nitride (hBN) layers and compared them with those samples prepared on SiO₂/Si substrates. We found that there is virtually no difference between the results for samples exfoliated directly on SiO₂/Si and those for samples on hBN/SiO₂/Si (see Supplementary Figs. 13 and 14), which strongly indicate that the extrinsic effect due to the substrate is not important.

Thickness dependence of QES signals. We further analyze the low-frequency QES signals due to the magnetic fluctuations^{23,26}. Since such QES signals are suppressed in the presence of the spin ordering in ferromagnetic or antiferromagnetic materials, its suppression can also be used as another good indicator for magnetic ordering. Figures 6a and 6b compare the temperature dependence of the low-frequency region of the polarized Raman spectra of 9L and monolayer NiPS₃. In parallel polarization configuration, the QES signals from 9L NiPS₃ are strongly suppressed below T_N , but a considerable amount of spectral weight persists down to the lowest

temperature in the case of monolayer NiPS₃. The difference is even more striking for the case of cross polarization configuration. Here, the QES signals from 9L NiPS₃ are somewhat enhanced near T_N , presumably because of strong spin fluctuations near the phase transition²⁷. On the other hand, the QES signals from monolayer NiPS₃ monotonically increase as the temperature is lowered as if it is approaching the phase transition. The temperature dependences of QES signals for intermediate thicknesses, such as 2L and 3L NiPS₃, are qualitatively similar to that of 9L NiPS₃ (see Supplementary Fig. 15). For a more quantitative analysis, the temperature dependence of the phonon population should be considered. Although the exact mechanism of QES in low-dimensional systems is not fully understood yet²³, we follow the theory of Reiter⁴¹ and Halley⁴² to analyze our data. The measured intensity of Stokes-shifted QES is simply expressed by⁴⁰⁻⁴⁵

$$I(\omega) \propto \frac{\omega}{1 - e^{-\hbar\omega/k_B T}} \frac{C_m T D k^2}{\omega^2 + (Dk^2)^2}, \quad (3)$$

where C_m is the magnetic specific heat and D is the thermal diffusion constant $D = K / C_m$ with the magnetic contribution to the thermal conductivity K . Since the Raman response $\chi''(\omega)$ for Stokes scattering is given by $\chi''(\omega) = I(\omega) / [n(\omega) + 1]$, where $n(\omega) = [\exp(\hbar\omega / k_B T) - 1]^{-1}$ is the Bose-Einstein factor, Eq. (3) is expressed in terms of the Raman response $\chi''(\omega)$ ^{40,45},

$$\frac{\chi''(\omega)}{\omega} \propto C_m T \frac{Dk^2}{\omega^2 + (Dk^2)^2}. \quad (4)$$

We obtained the spectral weight of QES by integrating the normalized Raman response χ'' / ω in the range of 11–40 cm⁻¹. Figure 6c shows the temperature dependence of the spectral weight of QES in both parallel- and cross-polarization configurations for several thicknesses. For both polarization configurations, the spectral weight of QES shows a peak near the magnetic transition temperature for all thicknesses except monolayer. In the case of monolayer NiPS₃, the spectral

weight of QES almost monotonically increases as the temperature is lowered in both polarization configurations as if it is approaching the phase transition from above. These results are consistent with our prior observation from the raw Raman data in Figs. 6a, b and support our interpretation that antiferromagnetic ordering is drastically suppressed in monolayer NiPS₃. The increase in the spectral weight of QES at low temperatures indicates that spin fluctuations in monolayer NiPS₃, most probably related to the bound vortex-antivortex pairs^{5,6}, are growing persistently as the temperature is decreasing even down to zero Kelvin.

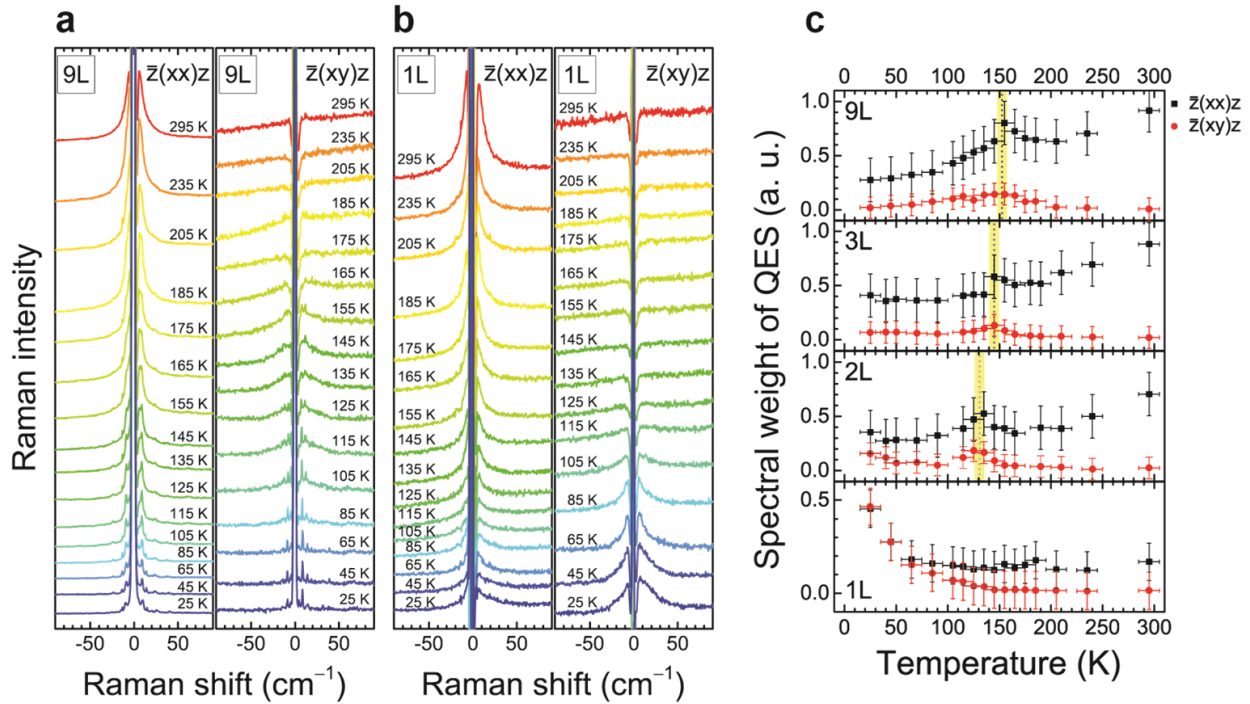


Fig. 6 Temperature dependence of quasi-elastic scattering signals. **a,b**, Low-frequency polarized Raman spectra of 9L (**a**) and monolayer (**b**) NiPS₃. **c**, Spectral weight of QES between 11 and 40 cm⁻¹ as a function of temperature for various thicknesses for parallel (black squares) and cross (red circles) polarization scattering configurations. The error bars indicate experimental uncertainties and dashed lines show estimated transition temperatures by using ΔP_2 .

Monte Carlo Simulations. In order to shed further light on the experimental observations, we have carried out Monte Carlo simulations as a function of the number of layers (see Supplementary Note 4 and Supplementary Fig. 16). The simulation results qualitatively support our interpretation of the experimental data. The simulated Néel temperature slowly decreases as the thickness is reduced, down to 2L case, but the decrease is more dramatic for monolayer. For a better quantitative agreement, more sophisticated calculations will be necessary, which is beyond the scope of this work.

Discussion

NiPS₃, an antiferromagnetic van der Waals material, is a good model system for the XY Hamiltonian. Using this material, we investigated the magnetic signals in the form of two-magnon and quasi-elastic scattering as a function of the sample thickness down to the monolayer limit. All our experimental observations coherently point to the conclusion that the antiferromagnetic ordering persists down to two-layer samples and is drastically suppressed in the monolayer. Furthermore, the Néel temperature is only slightly dependent on the number of layers as long as it is two or larger. This result is in stark contrast to the case of Ising-type antiferromagnet FePS₃, in which antiferromagnetic ordering persists down to the monolayer limit⁹. It is also different from the case of recently reported ferromagnetic 2D materials such as CrI₃ or Cr₂Ge₂Te₆, of which the Curie temperature decreases as the number of layers decreases but remains finite in the monolayer limit^{11,12}. The thickness dependence strongly indicates that the intra-layer exchange interactions are much stronger than the inter-layer ones. However, the inter-layer interaction suppresses the logarithmically divergent spin fluctuations, except in the monolayer. In monolayer NiPS₃, where the static and bulk antiferromagnetic order is suppressed by the strong fluctuations, there is the

low-temperature enhancement of quasi-elastic scattering. We note that all these experimental observations are in good agreement with the theoretical predictions of the XY model. Our work, one of the very rare experimental realizations of the XY Hamiltonian in the atomically thin monolayer limit, opens a new window of opportunities to study the extremely rich physics of the XY Hamiltonian and probably the BKT transition using a real material.

Methods

Sample preparation. NiPS₃ crystals were grown by chemical vapor transport reaction. Inside an argon-filled glove box, elemental powders (purchased from Sigma-Aldrich) of nickel (99.99% purity), phosphorus (99.99%) and sulfur (99.998%) were weighed and mixed in stoichiometric ratio 1:1:3 and an additional 5 wt-% of sulfur. The samples were immediately subjected to chemical analysis using a COXI EM-30 scanning electron microscope equipped with a Bruker QUANTAX 70 energy dispersive x-ray system to find the good stoichiometry of all the samples used in this study. The phase purity was further checked by taking powder X-ray diffraction (XRD) patterns with Bruker D8 Discover as well as single crystal XRD (XtaLAB P200, Rigaku) as shown in Supplementary Fig. 17. We further characterized the magnetic properties using a commercial setup (the SQUID magnetometer, Quantum Design) as shown in the Supplementary Fig. 2.

Few-layer NiPS₃ samples were prepared on Si substrates with a layer of 285-nm SiO₂ by mechanical exfoliation from a bulk single-crystal NiPS₃. Since few-layer NiPS₃ samples can be degraded in ambient conditions, the samples were kept in a vacuum desiccator to prevent possible degradations after exfoliation. All the measurements were carried out with the sample in vacuum in order to avoid any degradation during measurements. Atomic force microscopy images taken before and after Raman measurements confirmed that degradation is minimal as long as the sample

is kept in vacuum and the excitation laser intensity is kept at 100 μW or less (see Supplementary Note 5 and Supplementary Fig. 18 for details). The number of layers was determined based on the optical contrast¹⁹, atomic force microscopy, and low-frequency Raman measurements (see Supplementary Fig. 1).

Linear spin wave theory. The calculations of one-magnon spectrum were obtained by using SpinW package⁴⁶ for the zigzag magnetic ground state, assuming the following Hamiltonian:

$$\begin{aligned}
 H = & J_1 \sum_{\langle i,j \rangle} [S_i^x S_j^x + S_i^y S_j^y + \alpha S_i^z S_j^z] + J_2 \sum_{\langle\langle i,k \rangle\rangle} [S_i^x S_k^x + S_i^y S_k^y + \alpha S_i^z S_k^z] \\
 & + J_3 \sum_{\langle\langle\langle i,l \rangle\rangle\rangle} [S_i^x S_l^x + S_i^y S_l^y + \alpha S_i^z S_l^z] + \sum_i [D_1 (S_i^x)^2 + D_2 (S_i^z)^2] \quad , \quad (4)
 \end{aligned}$$

where the first three terms denote the XXZ Hamiltonian up to third nearest neighbor. The (x, y, z) coordinate system is defined with the known ordered moment of NiPS₃ in Supplementary Fig. 3c. The last terms in the bracket are single-ion anisotropy (SIA) along the x - and z -axis, respectively. Using the following set of parameters: $J_1 = 3.18$ meV, $J_2 = 4.82$ meV, $J_3 = 9.08$ meV, $\alpha = 0.66$, $D_1 = -0.89$ meV, $D_2 = 2.85$ meV, we calculated single magnon dispersion and then two-magnon continuum with the kinematic constraints. See Supplementary Information for further details.

Raman measurements. All the Raman measurements were carried out in vacuum using an optical cryostat (Oxford Microrstat He2) at temperatures from 10 to 295 K. The 514.4-nm (2.41 eV) line of diode-pumped-solid-state (DPSS) laser was used as the excitation source. The laser power was kept below 100 μW to avoid damaging the samples. The laser beam was focused onto the sample by a 40 \times microscope objective lens (0.6 N.A.), and the scattered light was collected and collimated by the same objective. The scattered signal was dispersed by a Jobin-Yvon Horiba iHR550 spectrometer (2400 grooves/mm) and detected with a liquid-nitrogen-cooled back-

illuminated charge-coupled-device (CCD) detector. Volume holographic filters (Ondax and Optigrate) were used to clean the laser lines and reject the Rayleigh-scattered light. For polarized Raman measurements, an achromatic half-wave plate was used to rotate the polarization of the incident linearly polarized laser beam. In addition, the analyzer angle was used to selectively pass scattered photons with parallel or cross polarizations. Another achromatic half-wave plate was placed in front of the entrance slit to keep the polarization direction of the signals entering the spectrometer constant with respect to the groove direction of the grating⁴⁷. The Raman spectrum of the substrate (SiO_2/Si) was measured from the same location without samples at each temperature and subtracted from the sample spectrum after normalization by the intensity of the 520 cm^{-1} silicon phonon peak. The temperature dependence of the Raman spectrum of a bulk NiPS_3 crystal was measured separately in a macro-Raman system by using a closed-cycle He cryostat. The excitation laser was focused by a spherical lens ($f=75 \text{ mm}$) to a spot of size $\sim 50 \mu\text{m}$ with a power of 2 mW.

Monte Carlo simulations. We calculated the zigzag-type antiferromagnetic order parameter and magnetic susceptibility in bulk and few-layer stacked honeycomb lattice by Monte Carlo simulations. We treated the spins classically and incorporated the short-range exchange interactions up to third neighbors with the anisotropy parameter α extracted from linear spin-wave theory as well as the inter-layer coupling. In Monte Carlo simulations we have performed importance sampling with Metropolis algorithm and used simulated annealing for finite-temperature calculation. Typically, at each temperature the first 10^5 Monte Carlo steps are discarded for equilibration and the following 10^6 Monte Carlo steps are used for averaging physical quantities. For all the numerical data from Monte Carlo simulations the numerical

uncertainties are smaller than or comparable to the size of symbols. See Supplementary Information for further details.

Density functional theory (DFT) phonon calculations. We calculated the phonon modes of monolayer NiPS₃ using density functional theory and frozen-phonon method. Vacuum layers of 12 Å thick were inserted between two adjacent monolayers of NiPS₃ to avoid spurious interactions between the periodic replicas. The lattice parameters and atomic coordinates were fully relaxed by using the Quantum ESPRESSO package⁴⁸. Ion-electron interactions were simulated by using norm-conserving pseudopotentials^{49,50}. The exchange-correlation energy was calculated by using the Perdew-Burke-Ernzerhof functional⁵¹. The kinetic energy cutoff was set to 80 Ry. The Brillouin-zone integrations were carried out by using the 6×6×1 Monkhorst-Pack grid⁵². The correlation effects of Ni 3*d* electrons were considered by using the density functional theory + U method⁵³. We used 4 eV for the effective Hubbard U of Ni 3*d* electrons. The phonon frequencies and eigenmodes were calculated by using the Phonopy package⁵⁴.

Data availability

The data that support the findings of this study are available from the corresponding authors upon request.

References

1. Onsager, L. Crystal Statistics. I. A Two-Dimensional Model with an Order-Disorder Transition. *Phys. Rev.* **65**, 117–149 (1944).
2. Hohenberg, P. C. Existence of Long-Range Order in One and Two Dimensions. *Phys. Rev.* **158**, 383–386 (1967).

3. Mermin, N. D. & Wagner, H. Absence of Ferromagnetism or Antiferromagnetism in One- or Two-Dimensional Isotropic Heisenberg Models. *Phys. Rev. Lett.* **17**, 1133–1136 (1966).
4. Coleman, S. There are no Goldstone bosons in two dimensions. *Commun. Math. Phys.* **31**, 259–264 (1973).
5. Berezinskii, V. Destruction of Long-range Order in One-dimensional and Two-dimensional Systems having a Continuous Symmetry Group I. Classical Systems. *Sov. Phys. JETP* **32**, 493 (1971).
6. Kosterlitz, J. M. & Thouless, D. J. Ordering, metastability and phase transitions in two-dimensional systems. *J. Phys. C Solid State Phys.* **6**, 1181–1203 (1973).
7. Mahan, G. D. *Condensed Matter in a Nutshell*. **96**, (Princeton University Press, 2011).
8. Taroni, A., Bramwell, S. T. & Holdsworth, P. C. W. Universal window for two-dimensional critical exponents. *J. Phys. Condens. Matter* **20**, 275233 (2008).
9. Lee, J.-U. *et al.* Ising-Type Magnetic Ordering in Atomically Thin FePS₃. *Nano Lett.* **16**, 7433–7438 (2016).
10. Wang, X. *et al.* Raman spectroscopy of atomically thin two-dimensional magnetic iron phosphorus trisulfide (FePS₃) crystals. *2D Mater.* **3**, 031009 (2016).
11. Gong, C. *et al.* Discovery of intrinsic ferromagnetism in two-dimensional van der Waals crystals. *Nature* **546**, 265–269 (2017).
12. Huang, B. *et al.* Layer-dependent ferromagnetism in a van der Waals crystal down to the monolayer limit. *Nature* **546**, 270–273 (2017).

13. Cuccoli, A., Roscilde, T., Tognetti, V., Vaia, R. & Verrucchi, P. Quantum Monte Carlo study of $S=1/2$ weakly anisotropic antiferromagnets on the square lattice. *Phys. Rev. B* **67**, 104414 (2003).
14. Cardy, J. *Scaling and Renormalization in Statistical Physics*. (Cambridge University Press, 1996).
15. Park, J.-G. Opportunities and challenges of 2D magnetic van der Waals materials: magnetic graphene? *J. Phys. Condens. Matter* **28**, 301001 (2016).
16. Burch, K. S., Mandrus, D. & Park, J.-G. Magnetism in two-dimensional van der Waals materials. *Nature* **563**, 47–52 (2018).
17. Joy, P. A. & Vasudevan, S. Magnetism in the layered transition-metal thiophosphates MPS_3 ($M = Mn, Fe, \text{ and } Ni$). *Phys. Rev. B* **46**, 5425–5433 (1992).
18. Wildes, A. R. *et al.* Magnetic structure of the quasi-two-dimensional antiferromagnet $NiPS_3$. *Phys. Rev. B* **92**, 224408 (2015).
19. Kuo, C.-T. *et al.* Exfoliation and Raman Spectroscopic Fingerprint of Few-Layer $NiPS_3$ Van der Waals Crystals. *Sci. Rep.* **6**, 20904 (2016).
20. Ferrari, A. C. & Basko, D. M. Raman spectroscopy as a versatile tool for studying the properties of graphene. *Nat. Nanotechnol.* **8**, 235–246 (2013).
21. Zhang, X. *et al.* Phonon and Raman scattering of two-dimensional transition metal dichalcogenides from monolayer, multilayer to bulk material. *Chem. Soc. Rev.* **44**, 2757–2785 (2015).
22. Fleury, P. A. & Loudon, R. Scattering of Light by One- and Two-Magnon Excitations. *Phys. Rev.* **166**, 514–530 (1968).

23. Lemmens, P., Güntherodt, G. & Gros, C. Magnetic light scattering in low-dimensional quantum spin systems. *Phys. Rep.* **375**, 1–103 (2003).
24. Susner, M. A., Chyashnavichyus, M., McGuire, M. A., Ganesh, P. & Maksymovych, P. Metal Thio- and Selenophosphates as Multifunctional van der Waals Layered Materials. *Adv. Mater.* **29**, 1602852 (2017).
25. Bernasconi, M. *et al.* Lattice dynamics of layered MPX₃ (M=Mn,Fe,Ni,Zn; X=S,Se) compounds. *Phys. Rev. B* **38**, 12089–12099 (1988).
26. Cottam, M. G. & Lockwood, D. J. *Light scattering in magnetic solids*. (Wiley, 1986).
27. Sekine, T., Jouanne, M., Julien, C. & Balkanski, M. Light-scattering study of dynamical behavior of antiferromagnetic spins in the layered magnetic semiconductor FePS₃. *Phys. Rev. B* **42**, 8382–8393 (1990).
28. Choi, K.-Y., Zvyagin, S. A., Cao, G. & Lemmens, P. Coexistence of dimerization and long-range magnetic order in the frustrated spin-chain system LiCu₂O₂: Inelastic light scattering study. *Phys. Rev. B* **69**, 104421 (2004).
29. Rosenblum, S., Francis, A. H. & Merlin, R. Two-magnon light scattering in the layered antiferromagnet NiPS₃: Spin-1/2-like anomalies in a spin-1 system. *Phys. Rev. B* **49**, 4352–4355 (1994).
30. Fano, U. Effects of Configuration Interaction on Intensities and Phase Shifts. *Phys. Rev.* **124**, 1866–1878 (1961).
31. Tan, P. H. *et al.* The shear mode of multilayer graphene. *Nat. Mater.* **11**, 294–300 (2012).
32. Oh, J. *et al.* Spontaneous decays of magneto-elastic excitations in non-collinear antiferromagnet (Y,Lu)MnO₃. *Nat. Commun.* **7**, 13146 (2016).

33. Toms, D. J. & O'Sullivan, W. J. Light scattering from two-magnon modes in K_2NiF_4 . *Solid State Commun.* **14**, 715–718 (1974).
34. Choi, K.-Y. *et al.* Anomalous orbital dynamics in LaSrMnO_4 observed by Raman spectroscopy. *Phys. Rev. B* **77**, 064415 (2008).
35. Tian, Y., Gray, M. J., Ji, H., Cava, R. J. & Burch, K. S. Magneto-elastic coupling in a potential ferromagnetic 2D atomic crystal. *2D Mater.* **3**, 025035 (2016).
36. Lee, J.-U., Park, J., Son, Y.-W. & Cheong, H. Anomalous excitonic resonance Raman effects in few-layered MoS_2 . *Nanoscale* **7**, 3229–3236 (2015).
37. del Corro, E. *et al.* Atypical Exciton–Phonon Interactions in WS_2 and WSe_2 Monolayers Revealed by Resonance Raman Spectroscopy. *Nano Lett.* **16**, 2363–2368 (2016).
38. Carvalho, B. R. *et al.* Intervalley scattering by acoustic phonons in two-dimensional MoS_2 revealed by double-resonance Raman spectroscopy. *Nat. Commun.* **8**, 14670 (2017).
39. Baltensperger, W. & Helman, J. S. Influence of magnetic order in insulators on the optical phonon frequency. *Helv. Phys. Acta* **41**, 668–673 (1968).
40. Choi, K.-Y., Lemmens, P. & Berger, H. Critical spin dynamics of the $S=1/2$ spin chain compound CuSe_2O_5 . *Phys. Rev. B* **83**, 174413 (2011).
41. Reiter, G. F. Light scattering from energy fluctuations in magnetic insulators. *Phys. Rev. B* **13**, 169–173 (1976).
42. Halley, J. W. Light Scattering as a Probe of Dynamical Critical Properties of Antiferromagnets. *Phys. Rev. Lett.* **41**, 1605–1608 (1978).
43. Yamada, I. & Onda, H. Light scattering from magnetic-energy fluctuations in the one-dimensional Heisenberg antiferromagnet KCuF_3 . *Phys. Rev. B* **49**, 1048–1053 (1994).

44. Lemmens, P. *et al.* Collective Singlet Excitations and Evolution of Raman Spectral Weights in the 2D Spin Dimer Compound $\text{SrCu}_2(\text{BO}_3)_2$. *Phys. Rev. Lett.* **85**, 2605–2608 (2000).
45. Glamazda, A., Lemmens, P., Do, S.-H., Choi, Y. S. & Choi, K.-Y. Raman spectroscopic signature of fractionalized excitations in the harmonic-honeycomb iridates β - and γ - Li_2IrO_3 . *Nat. Commun.* **7**, 12286 (2016).
46. Toth, S. & Lake, B. Linear spin wave theory for single-Q incommensurate magnetic structures. *J. Phys. Condens. Matter* **27**, 166002 (2015).
47. Yoon, D. *et al.* Strong polarization dependence of double-resonant Raman intensities in graphene. *Nano Lett.* **8**, 4270–4 (2008).
48. Giannozzi, P. *et al.* QUANTUM ESPRESSO: a modular and open-source software project for quantum simulations of materials. *J. Phys. Condens. Matter* **21**, 395502 (2009).
49. Hamann, D. R. Optimized norm-conserving Vanderbilt pseudopotentials. *Phys. Rev. B* **88**, 085117 (2013).
50. Schlipf, M. & Gygi, F. Optimization algorithm for the generation of ONCV pseudopotentials. *Comput. Phys. Commun.* **196**, 36–44 (2015).
51. Perdew, J. P., Burke, K. & Ernzerhof, M. Generalized Gradient Approximation Made Simple. *Phys. Rev. Lett.* **77**, 3865–3868 (1996).
52. Pack, J. D. & Monkhorst, H. J. Special points for Brillouin-zone integrations. *Phys. Rev. B* **16**, 1748–1749 (1977).
53. Dudarev, S. L., Botton, G. A., Savrasov, S. Y., Humphreys, C. J. & Sutton, A. P. Electron-energy-loss spectra and the structural stability of nickel oxide: An LSDA+U study. *Phys. Rev. B* **57**, 1505–1509 (1998).

54. Togo, A. & Tanaka, I. First principles phonon calculations in materials science. *Scr. Mater.* **108**, 1–5 (2015).

Acknowledgements

The authors thank insightful discussions with H.C. Lee, S. Yoon, K. Burch, A. Wildes, and K.-Y. Choi. We are also grateful to S. Kang for his low-temperature single crystal X-ray diffraction experiments. This work was supported by the National Research Foundation (NRF) grants funded by the Korean government (MSIT) (NRF-2016R1A2B3008363, NRF-2017H1A2A1047040, No.2016R1A1A1A05919979 and, No.2017R1A5A1014862, SRC program: vdWMRC center), by a grant (2013M3A6A5073173) from the Center for Advanced Soft Electronics under the Global Frontier Research Program of MSIT, and by the Creative-Pioneering Research Program through Seoul National University. Computational resources have been provided by KISTI Supercomputing Center (KSC-2017-S1-0011). Work at IBS CCES was supported by Institute for Basic Science (IBS) in Korea (IBS-R009-G1).

Author Contributions

J.-G.P. and H.C. conceived the experiments. S.L. grew bulk NiPS₃ crystals. K.K., S.Y.L., and J.-U.L. carried out Raman measurements. K.P. performed spin wave calculations. T.Y.K. carried out first-principles phonon calculations. G.S.J. conducted Monte Carlo simulations. All authors discussed the data and wrote the manuscript together.

Additional information

Supplementary Information accompanies this paper at <http://doi.org/10.1038/XXXXXXX>.

Competing interests: The authors declare no competing interests.

Reprints and permissions information is available online at

<http://npag.nature.com/reprintsandpermissions/>

Publisher's note: Springer Nature remains neutral with regard to jurisdictional claims in published maps and institutional affiliations.

Supplementary Information

Suppression of magnetic ordering in XXZ-type antiferromagnetic monolayer NiPS₃

*Kangwon Kim,[†] Soo Yeon Lim,[†] Jae-Ung Lee,[†] Sungmin Lee,^{‡,§} Tae Yun Kim,^{§,¶} Kisoo Park,^{‡,§}
Gun Sang Jeon,[#] Cheol-Hwan Park,^{§,¶,*} Je-Geun Park,^{‡,§,*} and Hyeonsik Cheong^{†,*}*

[†]Department of Physics, Sogang University, Seoul 04107, Korea

[‡]Center for Correlated Electron Systems, Institute for Basic Science, Seoul 08826, Korea

[§]Department of Physics and Astronomy, Seoul National University, Seoul 08826, Korea

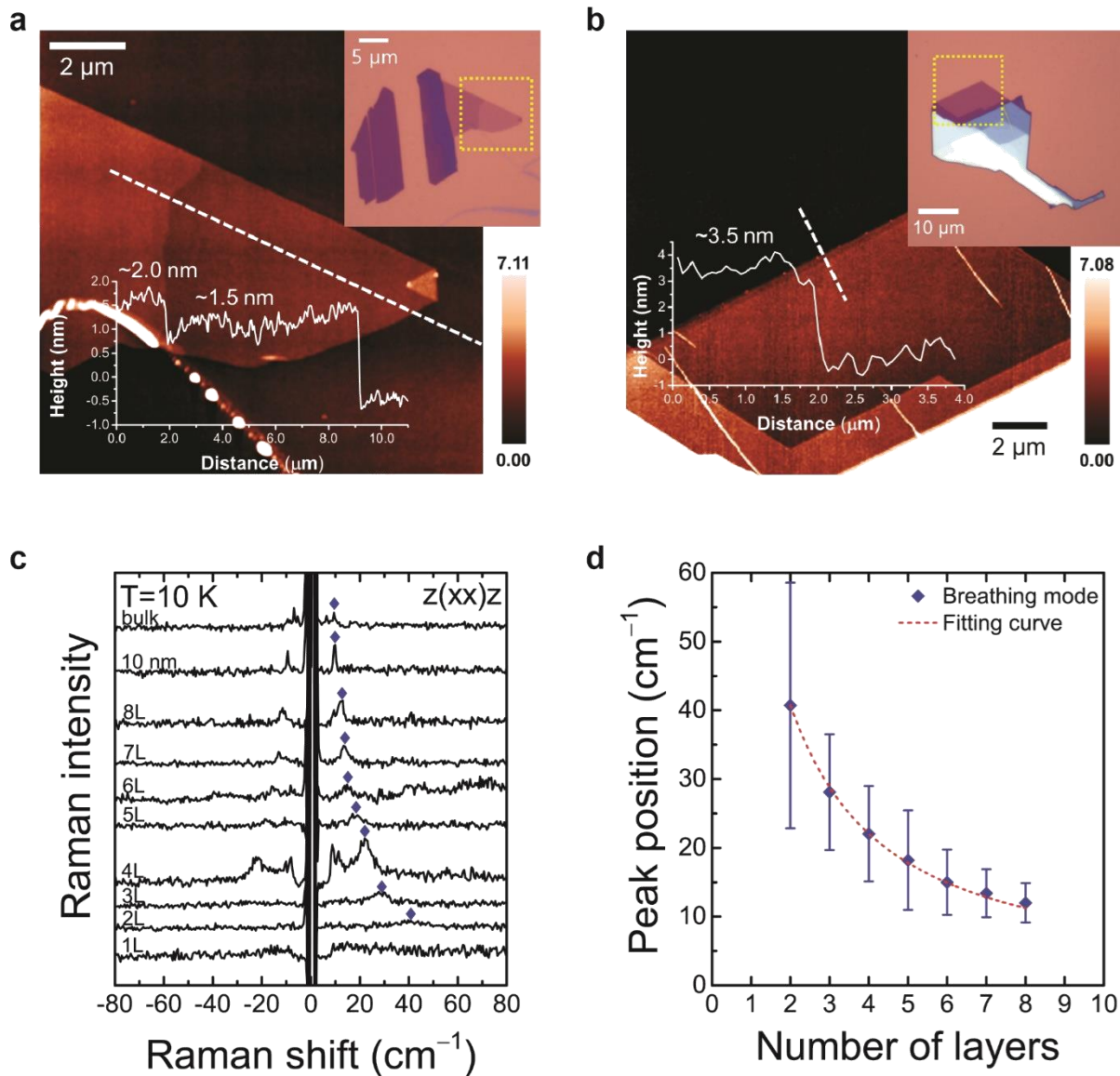
[¶]Center for Theoretical Physics, Seoul National University, Seoul 08826, Korea

[#]Department of Physics, Ewha Womans University, Seoul 03760, Korea

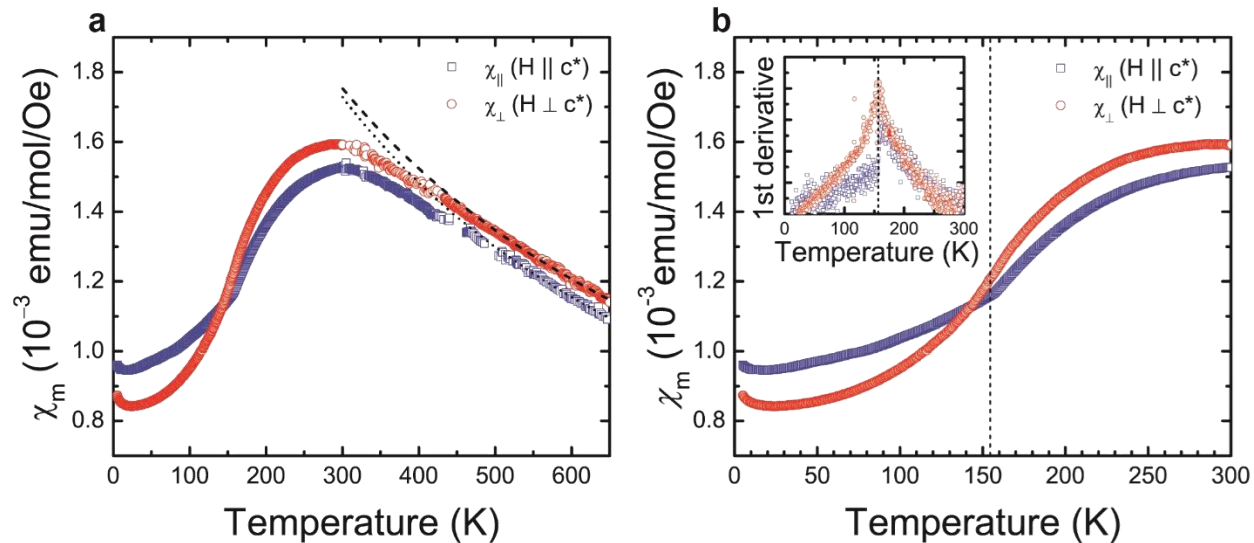
Χοντεντο:

- **Supplementary Figure 1.** Determination of the sample thickness.
- **Supplementary Figure 2.** Magnetic susceptibility of single crystal NiPS₃.
- **Supplementary Note 1.** Calculation of two-magnon density of states (DOS).
- **Supplementary Figure 3.** Comparison of two-magnon signals of Raman with theoretical calculation of two-magnon DOS.
- **Supplementary Table 1.** Experimental peak positions and calculated phonon frequencies of Raman-active modes of bulk NiPS₃ with zigzag antiferromagnetic ordering.
- **Supplementary Figure 4.** Comparison of calculated phonon frequencies with experimental spectra.

- **Supplementary Figure 5.** Temperature dependence of P_5 and P_7 in bulk NiPS_3
- **Supplementary Figure 6.** Temperature dependence of Raman spectra of 10 nm, 8L, 4L, 3L, and 2L NiPS_3 in cross-polarization scattering configuration.
- **Supplementary Figure 7.** Polarization dependence of Raman spectra of bulk NiPS_3 .
- **Supplementary Figure 8.** Thickness dependence of polarized Raman spectra.
- **Supplementary Note 2.** Origin of P_3 at $\sim 210 \text{ cm}^{-1}$ in few-layer NiPS_3 .
- **Supplementary Figure 9.** Excitation energy dependence of Raman spectra of 1-3L and bulk NiPS_3 .
- **Supplementary Figure 10.** Temperature dependence of P_3 .
- **Supplementary Figure 11.** Polarized Raman spectra of 10 nm, 8L, 4L, 3L, 2L, and 1L NiPS_3 in parallel- and cross-polarization configurations as a function of temperature.
- **Supplementary Note 3.** Extracting transition temperature by using ΔP_2 .
- **Supplementary Figure 12.** Extracting transition temperature by using ΔP_2 .
- **Supplementary Figure 13.** Comparison of substrate effects.
- **Supplementary Figure 14.** ΔP_2 in NiPS_3 on hexagonal boron nitride (hBN).
- **Supplementary Figure 15.** Temperature dependence of quasi-elastic scattering signals.
- **Supplementary Note 4.** Monte Carlo simulations.
- **Supplementary Figure 16.** Results of Monte Carlo simulations.
- **Supplementary Figure 17.** X-ray diffraction patterns of NiPS_3 single crystal.
- **Supplementary Note 5.** Degradation test for few-layer NiPS_3
- **Supplementary Figure 18.** Photo-degradation test for few-layer NiPS_3 .



Supplementary Figure 1 | Determination of the sample thickness. **a,b**, Atomic force microscopy images of 2L, 3L (**a**), and 4L (**b**) NiPS₃. The insets are optical microscope images. **c**, Thickness dependence of low-frequency Raman spectra of few-layer NiPS₃ at $T=10$ K. **d**, Position of the breathing mode as a function of the number of layers. The error bars indicate uncertainties due to the peak widths in the spectra. The broken curve is fitting to the linear chain model^{1,2}.



Supplementary Figure 2 | Magnetic susceptibility of single crystal NiPS₃. The dashed and dotted curves represent the Curie-Weiss fitting results in **a**. The inset of **b** is the first derivative of the magnetic susceptibility. The peak corresponds to the Néel temperature.

● Supplementary Note 1

Calculation of two-magnon density of states (DOS)

We carried out spin waves calculations to explain the two-magnon continuum found in our Raman data of NiPS₃. In order to have the zigzag-type magnetic structure as obtained from neutron diffraction studies^{3,4}, we used a J_1 - J_2 - J_3 Heisenberg Hamiltonian for the honeycomb lattice. According to previous theoretical studies⁵⁻⁸ of the J_1 - J_2 - J_3 model, the zigzag magnetic structure can be stabilized by considering up to third-nearest neighbor interaction (J_3). For example, when there is an antiferromagnetic J_1 , a zigzag magnetic structure has been found if both J_2 and J_3 are larger than $0.6 J_1$. To be consistent with the experimental evidence suggesting the XY symmetry in the physical properties of NiPS₃, we used the following J_1 - J_2 - J_3 XXZ Hamiltonian as given below:

$$\begin{aligned}
 H = & J_1 \sum_{\langle i,j \rangle} \left[S_i^x S_j^x + S_i^y S_j^y + \alpha S_i^z S_j^z \right] + J_2 \sum_{\langle\langle i,k \rangle\rangle} \left[S_i^x S_k^x + S_i^y S_k^y + \alpha S_i^z S_k^z \right] \\
 & + J_3 \sum_{\langle\langle\langle i,t \rangle\rangle\rangle} \left[S_i^x S_t^x + S_i^y S_t^y + \alpha S_i^z S_t^z \right] + \sum_i \left[D_1 (S_i^x)^2 + D_2 (S_i^z)^2 \right]
 \end{aligned} \tag{1}$$

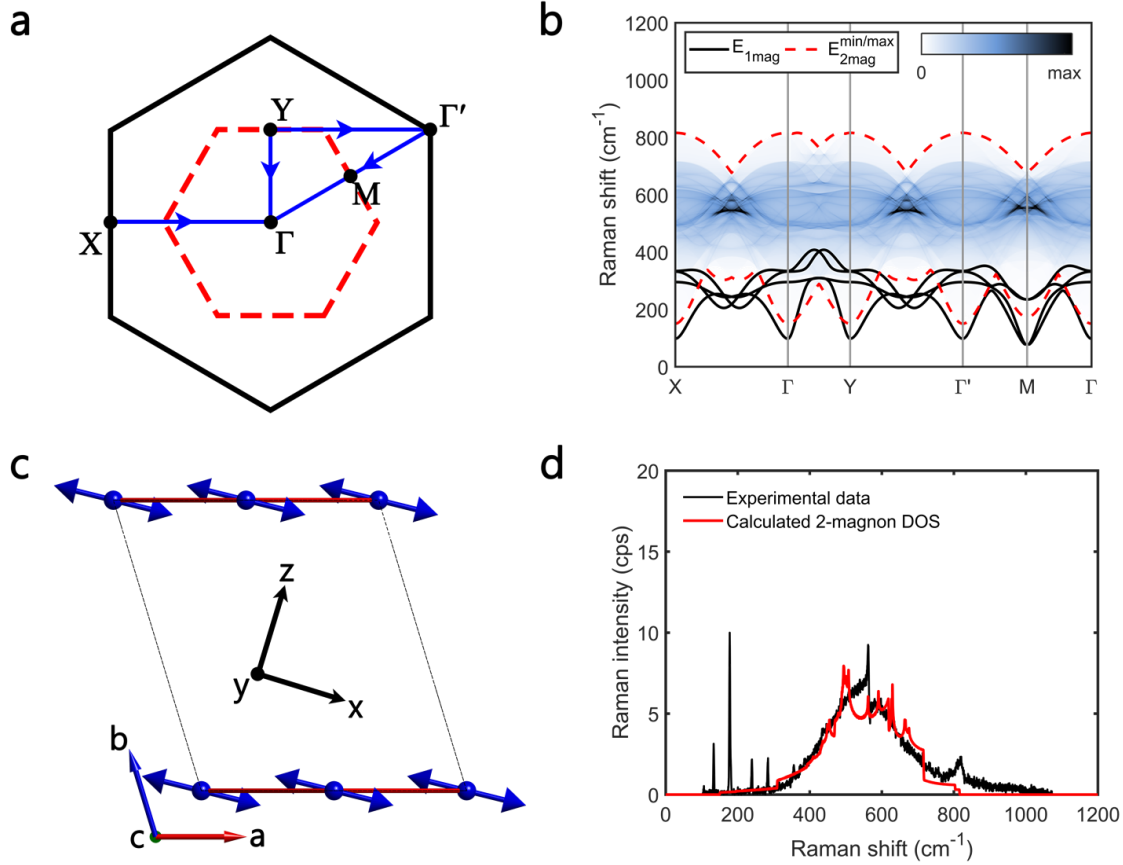
First three terms denote the XXZ anisotropic Hamiltonian up to third nearest neighbors with an anisotropy parameter α . The local (x, y, z) coordinates are defined consistently with the magnetic structure of NiPS₃ in Supplementary Fig. 3c. The last terms in the bracket are single-ion anisotropies (SIA) along the x - and z -axes, respectively. We neglected an inter-layer coupling as it is known to be smaller by two orders of magnitude than the intra-layer coupling^{9,10}.

Two-magnon spectrum measured by Raman scattering corresponds to the sum of the two single-magnon with a total momentum of $\mathbf{q} = 0$. In the magnetic system with negligible magnon-magnon interaction, two-magnon density of states (DOS) can be directly related to the Raman intensity¹¹. We calculated the two-magnon DOS in the following way. First, for a given \mathbf{k} point of the two magnon continuum a one-magnon dispersion was calculated at randomly chosen one million sample \mathbf{q} points using the SpinW software¹². After that, two-magnon DOS was calculated with the following sum rule satisfying kinematic constraints:

$$D_{\mathbf{k}}(\varepsilon_{\mu\mathbf{k}}) = \pi \sum_{\mathbf{q}, m} \delta(\varepsilon_{\mu\mathbf{k}} - \varepsilon_{m\mathbf{q}} - \varepsilon_{n\mathbf{k}-\mathbf{q}}), \tag{2}$$

where $\varepsilon_{\mu\mathbf{k}}$ is the dispersion of the μ -th magnon band.

We employed a particle swarm optimization algorithm to find the global minimum in the parameter space to explain the two-magnon continuum observed by our Raman data. The best fitting results were achieved with the following set of parameters: $J_1 = 3.18$ meV, $J_2 = 4.82$ meV, $J_3 = 9.08$ meV, $\alpha = 0.66$, $D_1 = -0.89$ meV, $D_2 = 2.85$ meV (see Supplementary Figs. 3b and 3d).

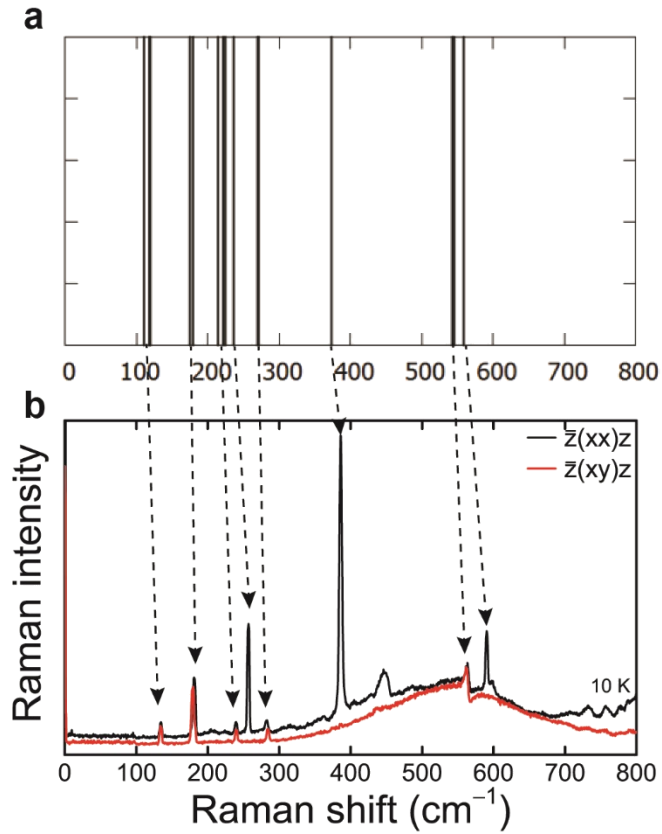


Supplementary Figure 3 | Comparison of two-magnon signals of Raman with theoretical calculations of two-magnon DOS. a, Schematic diagram for the 1st Brillouin zone with several symmetry points marked. **b**, Spin wave dispersion. **c**, Magnetic structure of antiferromagnetic NiPS₃. **d**, Comparison of experimental and theoretical two-magnon continuum.

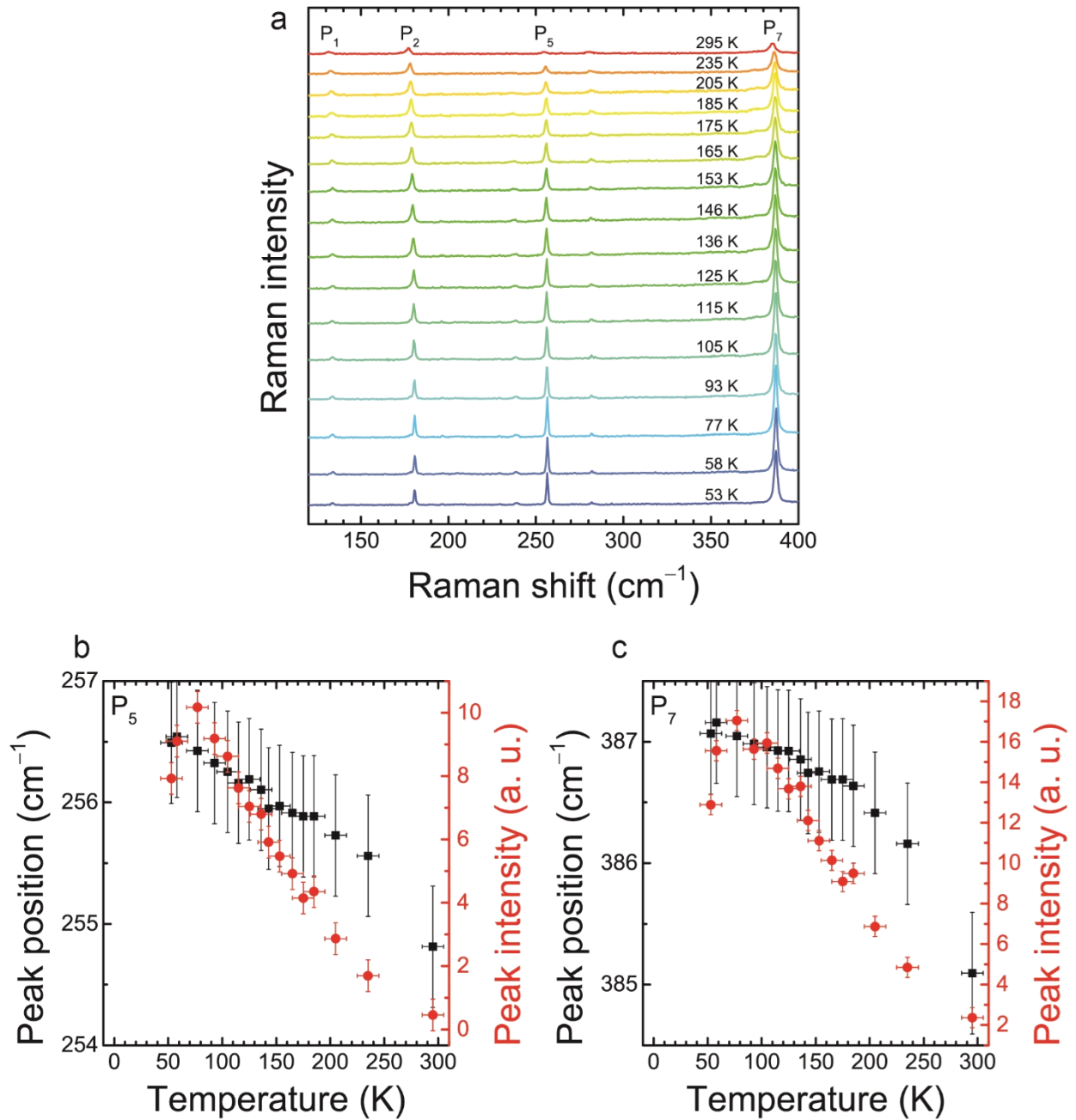
Supplementary Table 1 | Experimental peak positions and calculated phonon frequencies of Raman-active modes of bulk NiPS₃ with zigzag antiferromagnetic ordering.

<i>Peak</i>	<i>Experimental (cm⁻¹)</i>	<i>Calculation (cm⁻¹)</i>	<i>Mode (C_{2h})</i>	<i>Mode (D_{3d})*</i>
		111.04	<i>B_g</i>	
<i>P₁</i>	133.8	117.28	<i>A_g</i>	<i>E_g</i>
	134.9	118.71	<i>B_g</i>	
<i>P₂</i>	179.0	174.35	<i>A_g</i>	<i>E_g</i>
	181.3	179.42	<i>B_g</i>	
		213.65	<i>B_g</i>	
<i>P₃</i>	206.7			
<i>P₄</i>	239.6	221.82	<i>A_g</i>	<i>E_g</i>
	240.1	224.12	<i>B_g</i>	
<i>P₅</i>	256.9	235.56	<i>A_g</i>	<i>A_g</i>
<i>P₆</i>	282.3	269.88	<i>B_g</i>	<i>E_g</i>
	284.4	270.48	<i>A_g</i>	
<i>P₇</i>	386.1	372.62	<i>A_g</i>	<i>A_g</i>
<i>P₈</i>	446.8			
<i>P₉</i>	564.2	543.47	<i>A_g</i>	<i>E_g</i>
	565.6	545.07	<i>B_g</i>	
<i>P₁₀</i>	590.5	559.25	<i>A_g</i>	<i>A_g</i>

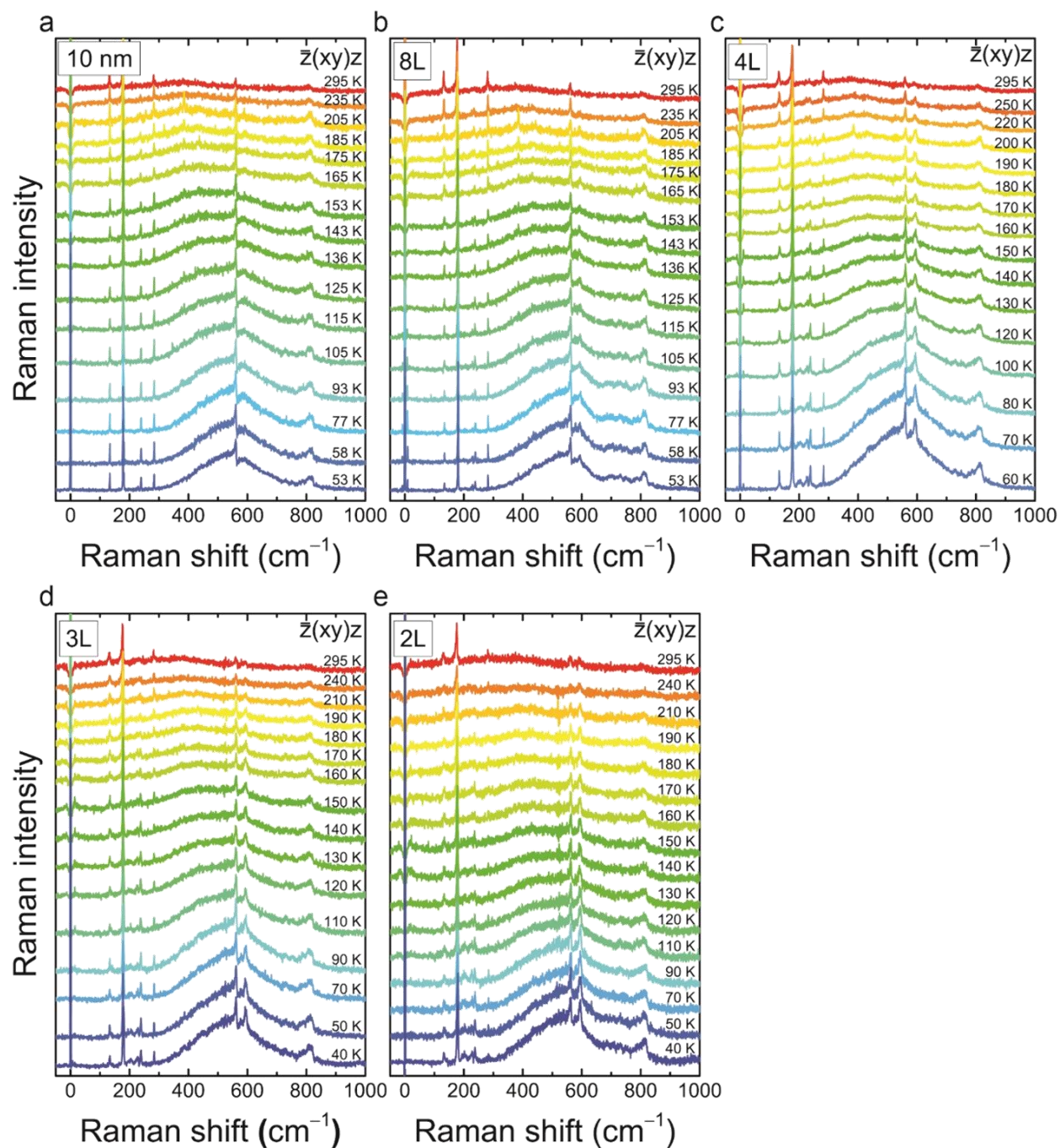
* Approximate corresponding mode in the *D_{3d}* point group of monolayer NiPS₃.



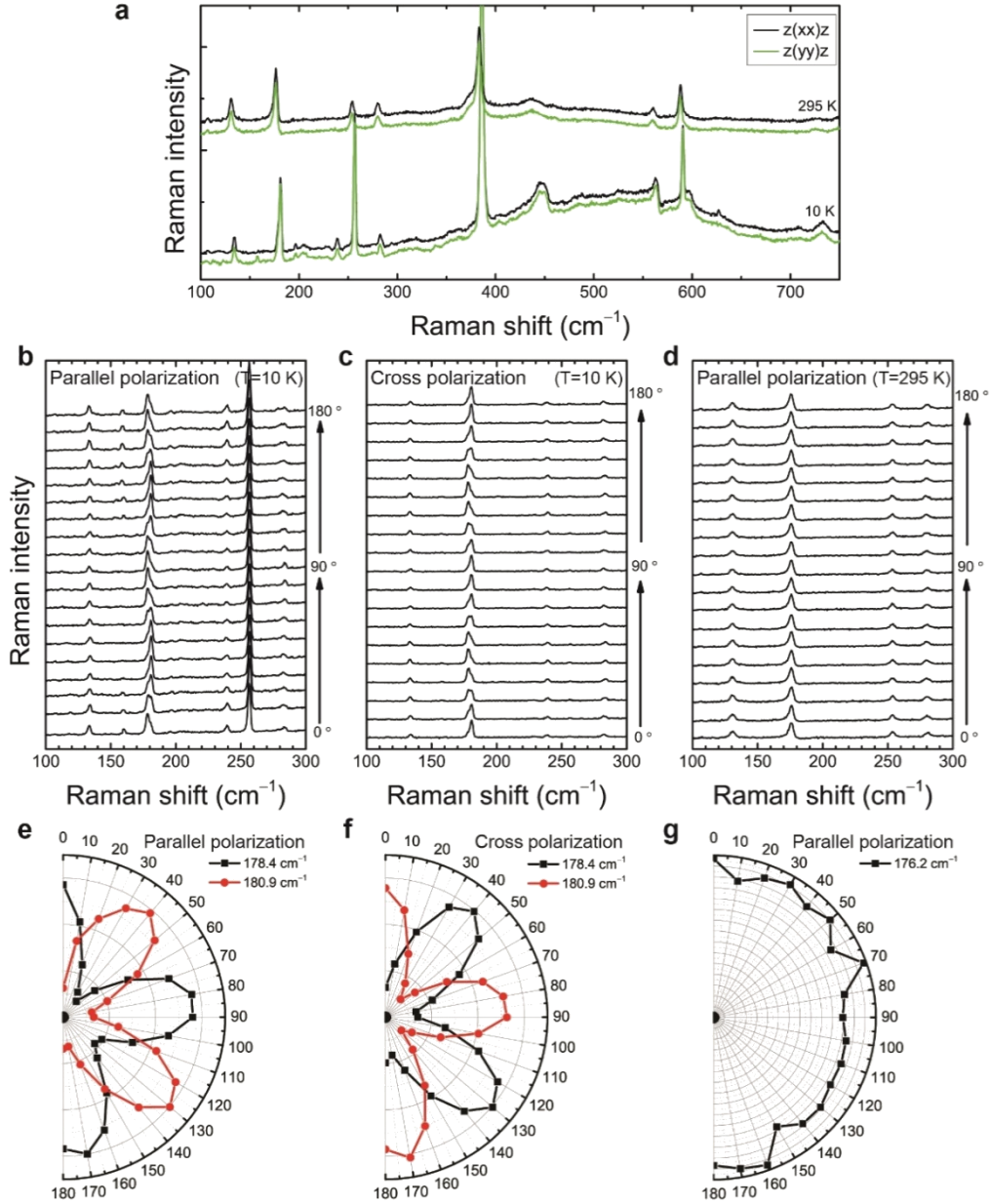
Supplementary Figure 4 | Comparison of calculated phonon frequencies with experimental spectra. a,b, Calculated phonon frequencies of Raman-active modes (a) and experimental Raman spectra (b) of bulk NiPS₃ with zigzag antiferromagnetic ordering.



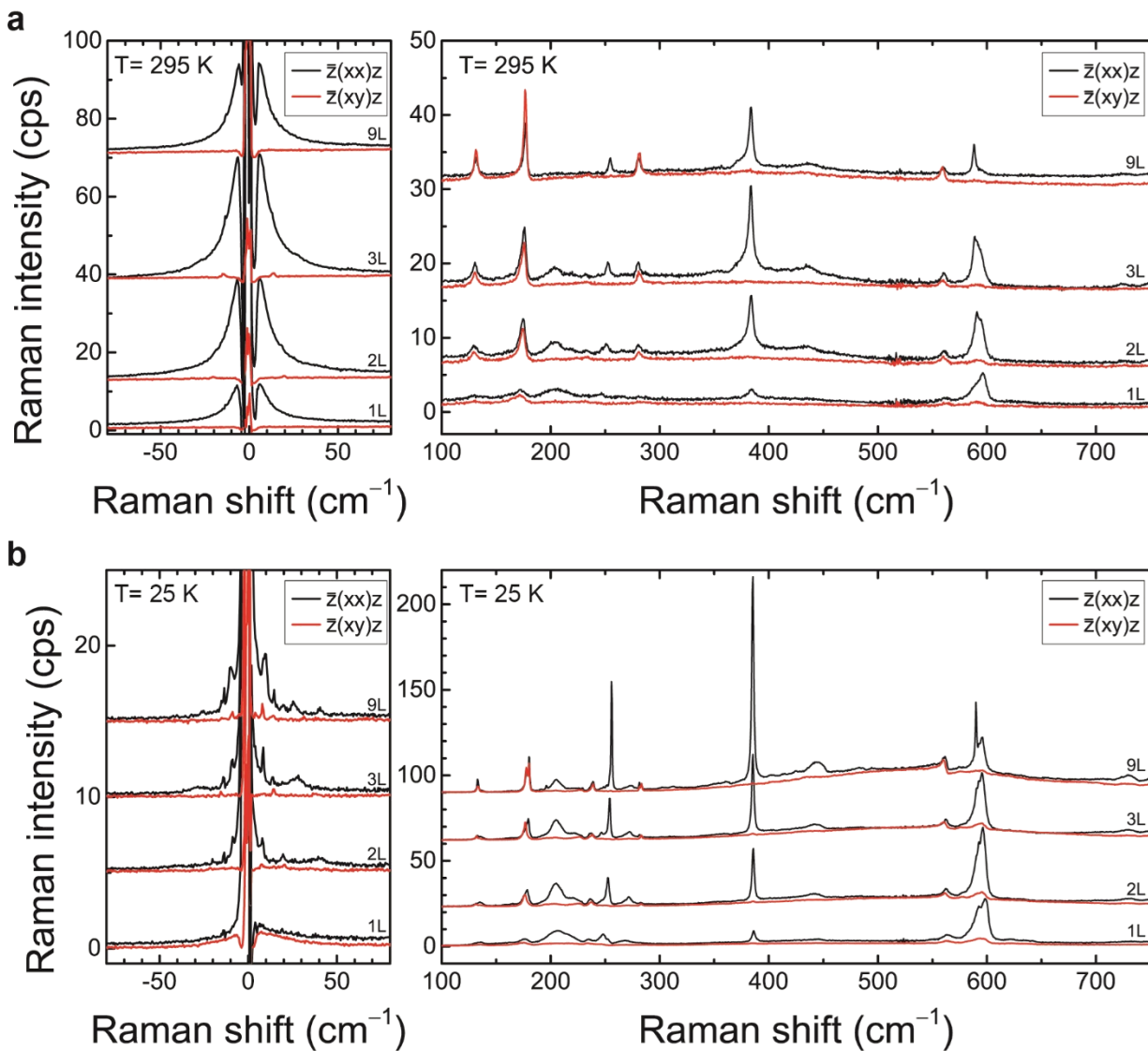
Supplementary Figure 5 | Temperature dependence of P_5 and P_7 in bulk NiPS_3 . **a**, Temperature dependent Raman spectra of bulk NiPS_3 in $\bar{z}(xx)z$ polarization configuration. **b,c**, Temperature dependence of peak position and intensity of P_5 (**b**) and P_7 (**c**). The error bars indicate experimental uncertainties.



Supplementary Figure 6 | Temperature dependence of two-magnon signal and Fano resonance of P9. a–e, Raman spectra of 10 nm (a), 8L (b), 4L (c), 3L (d), and 2L (e) NiPS₃ as a function of temperature obtained by using cross-polarization configuration.



Supplementary Figure 7 | Polarization dependence of P₂. **a**, Comparison of Raman spectra of bulk NiPS₃ obtained by using $\bar{z}(xx)z$ and $\bar{z}(yy)z$ polarization configurations shows that x and y directions are equivalent. **b–d**, Polarized Raman spectra as a function of the incident polarization direction for parallel (**b**) and cross (**c**) polarization configurations at $T=10$ K and for parallel (**d**) polarization configuration at $T=295$ K. **e–g**, Intensities of P₂ as a function of polarization at $T=10$ K in parallel (**e**) and cross (**f**) polarization configurations and at 295 K (**g**) in parallel-polarization configuration.



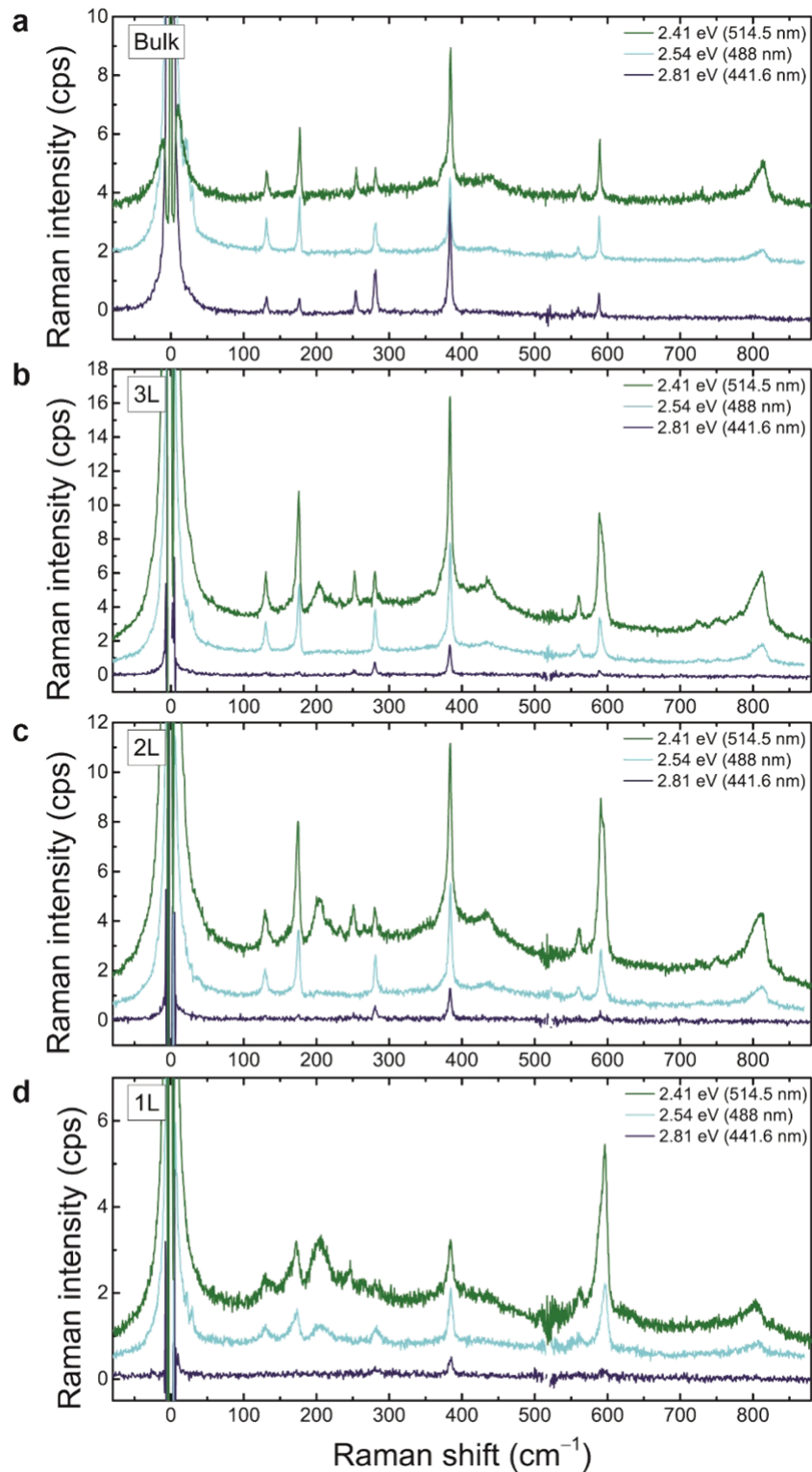
Supplementary Figure 8 | Thickness dependence of polarized Raman spectra. a,b, Polarized Raman spectra of 1L, 2L, 3L, and 9L at $T=295$ K (a), and $T=25$ K (b) in parallel and cross polarization configurations.

● Supplementary Note 2.

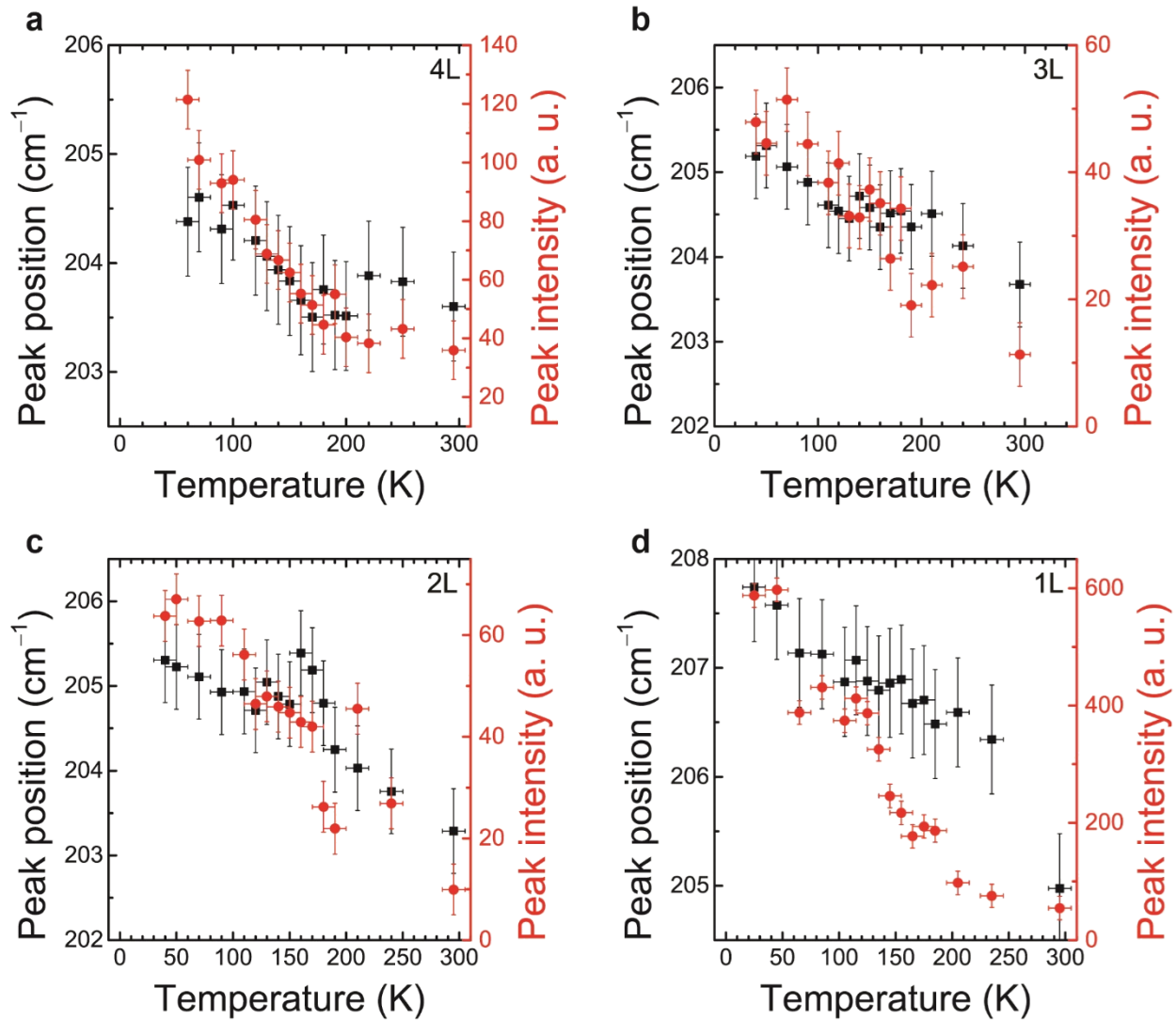
Origin of P_3 at $\sim 210\text{ cm}^{-1}$ in few-layer NiPS_3

A broad and strong peak (P_3) near 210 cm^{-1} is absent in bulk but appears in the spectrum of few-layer NiPS_3 (see Supplementary Fig. 8). We interpret that this peak is due to resonance-enhanced multiphonon scattering that is frequently observed in many 2-dimensional materials such as MoS_2 and WS_2 ^{13,14}. For example, in MoS_2 , the signal from 2-phonon scattering of zone-boundary longitudinal acoustic phonons (2LA) is strongly enhanced for resonant excitation of 1.96 eV and dominates the spectrum, with an intensity much larger than the main Raman-active zone-center optical phonon modes. This phenomenon has been explained in terms of the interplay between the large densities of states of the zone-boundary phonons and the electronic bands that are resonant with the excitation laser¹⁷.

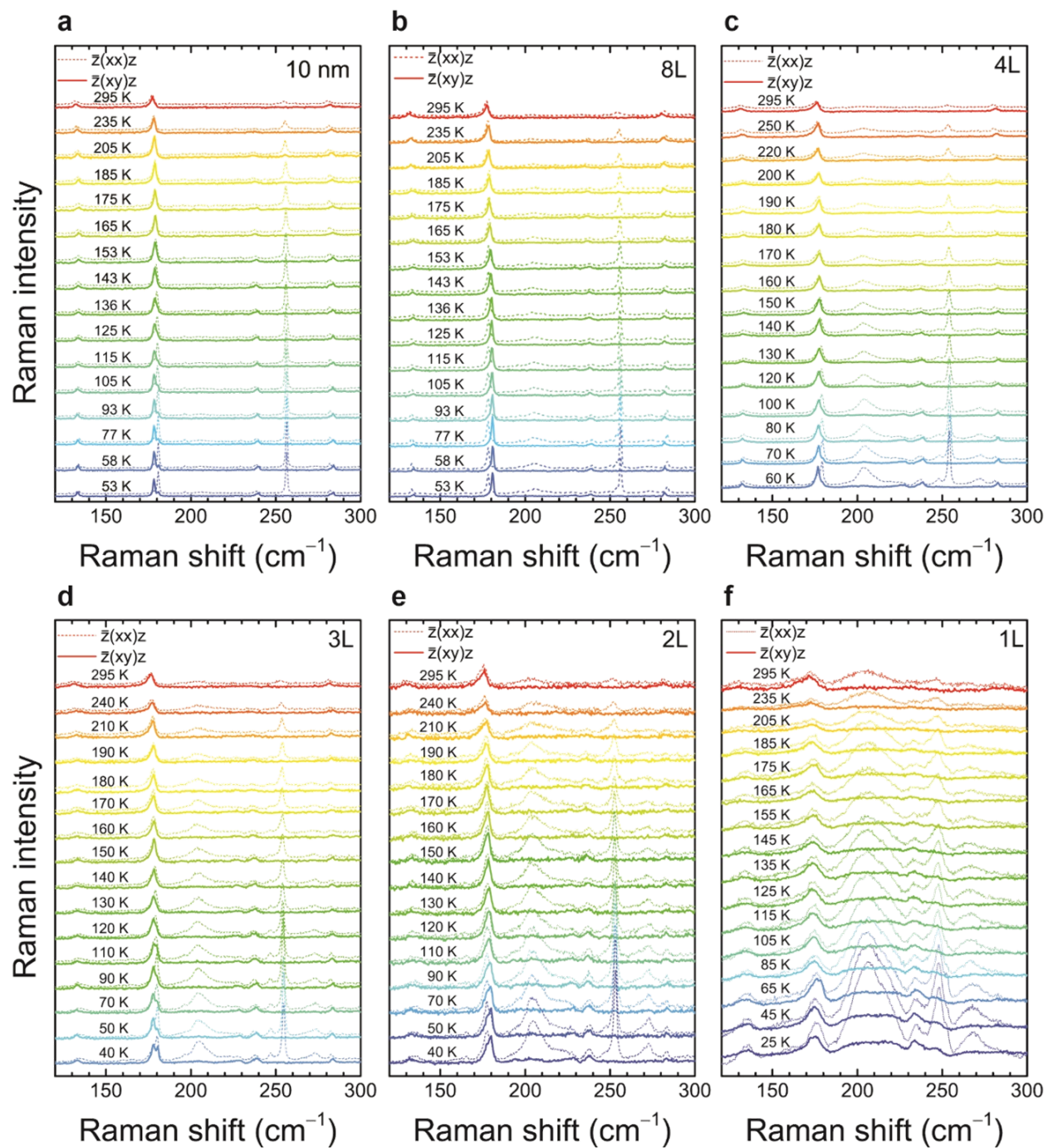
In the case of NiPS_3 , theoretical calculations by M. Bernasconi *et al.*¹⁵ predicts that the phonon density of modes is very large near 105 cm^{-1} due to multiple phonon branches near the K point of the Brillouin zone. Resonant enhancement of two-phonon scattering involving these phonons would explain the observed peak at 210 cm^{-1} . In order to verify this interpretation, we carried out Raman measurements on 1-3L and bulk NiPS_3 samples using several lasers. As seen in Supplementary Fig. 9, P_3 is present in 1-3L but absent in bulk NiPS_3 when the 2.41-eV excitation is used. When the excitation energy is slightly increased to 2.54 eV, P_3 disappears for 2L and 3L and is significantly decreased for 1L. The intensities of the other peaks also decrease, indicating that we are moving away from the resonance, but P_3 is preferentially suppressed, supporting our hypothesis that this peak is preferentially enhanced due to a special resonance conditions. For the 2.81-eV excitation, P_3 is completely suppressed for all samples, but other peaks are also greatly diminished. These observations support our interpretation that this peak originates from two-phonon scattering strongly enhanced by resonance effects.



Supplementary Figure 9 | Excitation energy dependence of Raman spectra of 1-3L and bulk NiPS₃. Unpolarized Raman spectra measured at room temperature by using the 2.41, 2.54, and 2.81 eV excitation energies for bulk (a), 3L (b), 2L (c), 1L (d) NiPS₃.



Supplementary Figure 10 | Temperature dependence of P₃. a-d, Temperature dependence of peak position and intensity for 4L (a), 3L (b), 2L (c), and 1L (d). The error bars indicate experimental uncertainties. No correlation with the magnetic transition is seen.



Supplementary Figure 11 | Temperature dependence of ΔP_2 . a–f, Polarized Raman spectra of 10 nm (a), 8L (b), 4L (c), 3L (d), 2L (e), and 1L (f) NiPS₃ obtained by using parallel- and cross-polarization configurations as a function of temperature.

● **Supplementary Note 3.**

Extracting transition temperature by using ΔP_2

Baltensperger and Helman¹⁶ developed a general theory of the spin-induced phonon frequency shift in magnetic crystals. The Hamiltonian in a magnetic crystal is expressed by $H = H^l + H^m$, where H^l is the pure lattice energy including anharmonic terms and H^m is the spin dependent phonon energy, expressed by

$$H_m = \sum_{i < j} I_{ij} S_i \cdot S_j, \quad (3)$$

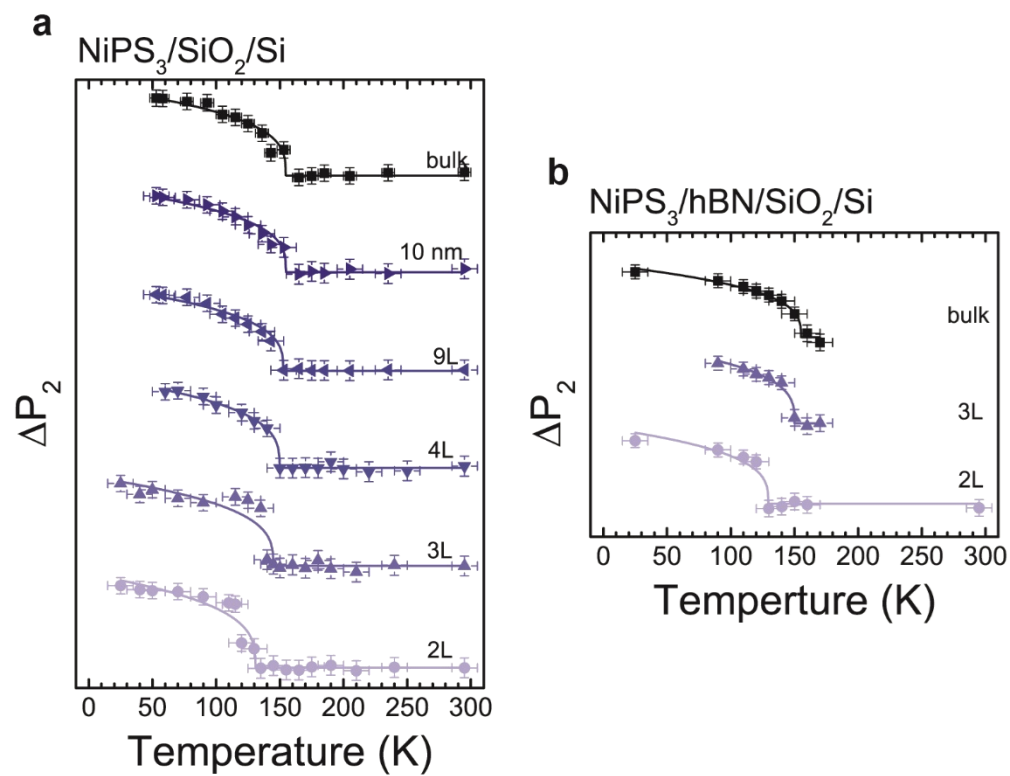
where I_{ij} is the superexchange coupling constant between magnetic ions i, j ; and S the ion spin operator. By solving the Hamiltonian, we can obtain the spin-induced phonon frequency which is simply expressed by $\Delta\omega \sim \langle S_0 \cdot S_1 \rangle / S^2$, where $\langle S_0 \cdot S_1 \rangle / S^2$ is the nearest neighbor spin correlation function. Near the phase transition temperature, the spin correlation function can be approximated as^{17,18}

$$\langle S_0 \cdot S_1 \rangle / S^2 \sim m^2(T) \sim (T_N - T)^{2\beta}. \quad (4)$$

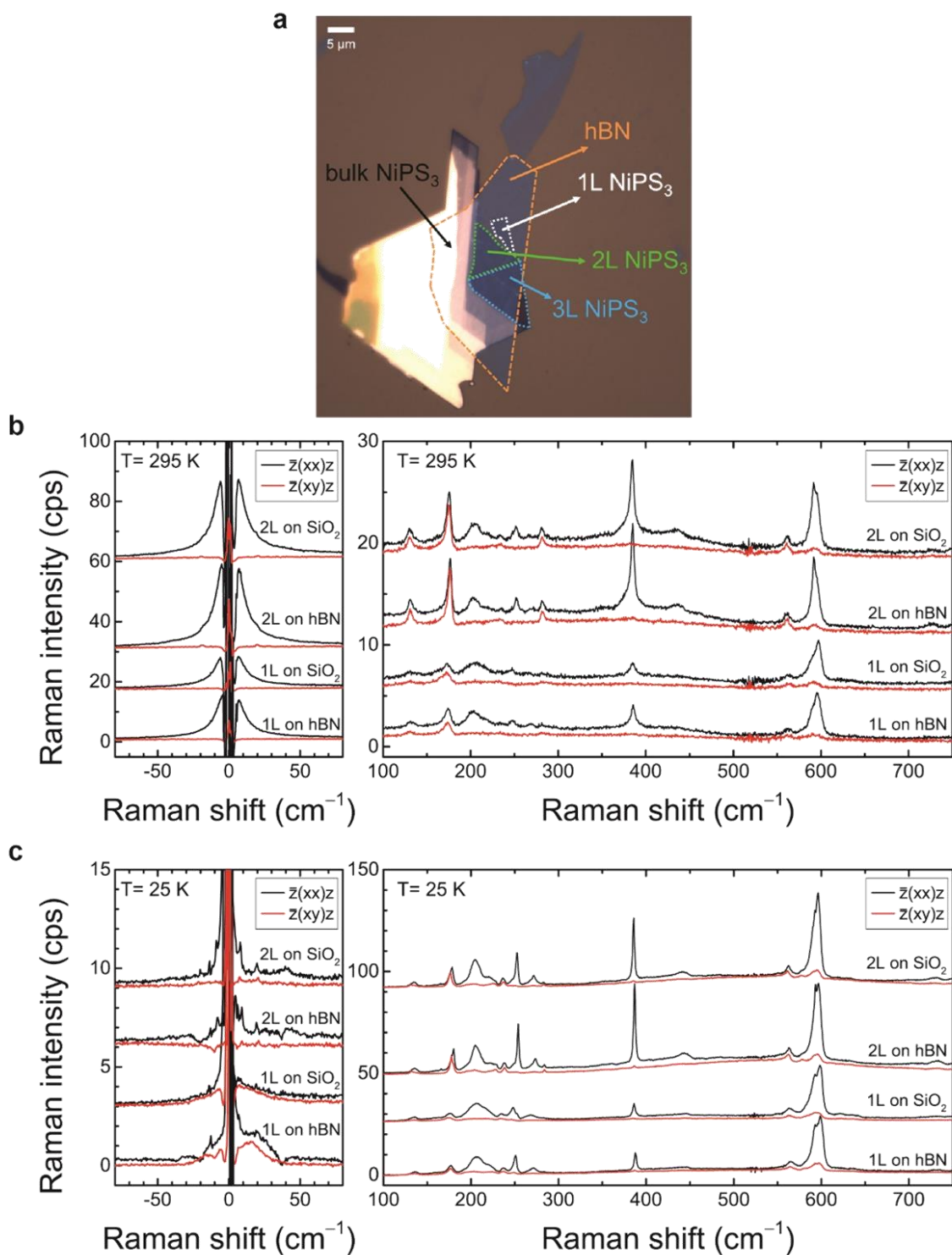
Therefore, the difference of phonon energy between P₂ is simply expressed by

$$\Delta\omega_{P_2} \sim \left| M \langle S_0 \cdot S_1 \rangle / S^2 \right| \sim A(T_N - T)^{2\beta}. \quad (5)$$

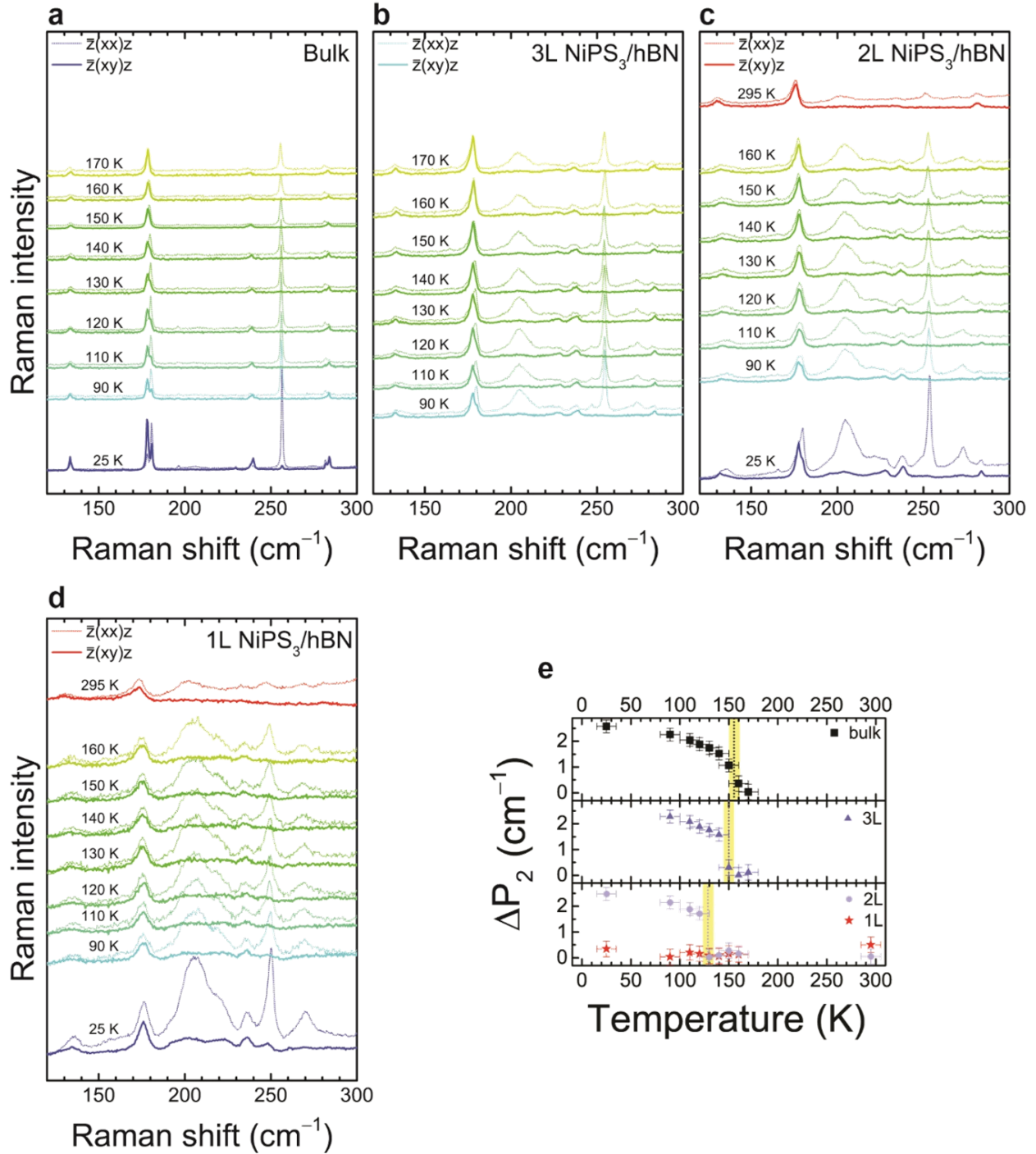
By assuming that the critical exponent is the same regardless of thickness, the magnetic transition temperature and the critical exponent can be estimated by fitting the data to Eq. (5). This yields $\beta \sim 0.16$ which is consistent with neutron scattering results⁴ on bulk NiPS₃. In Supplementary Fig. 12, the experimental data and the fitting curves are compared.



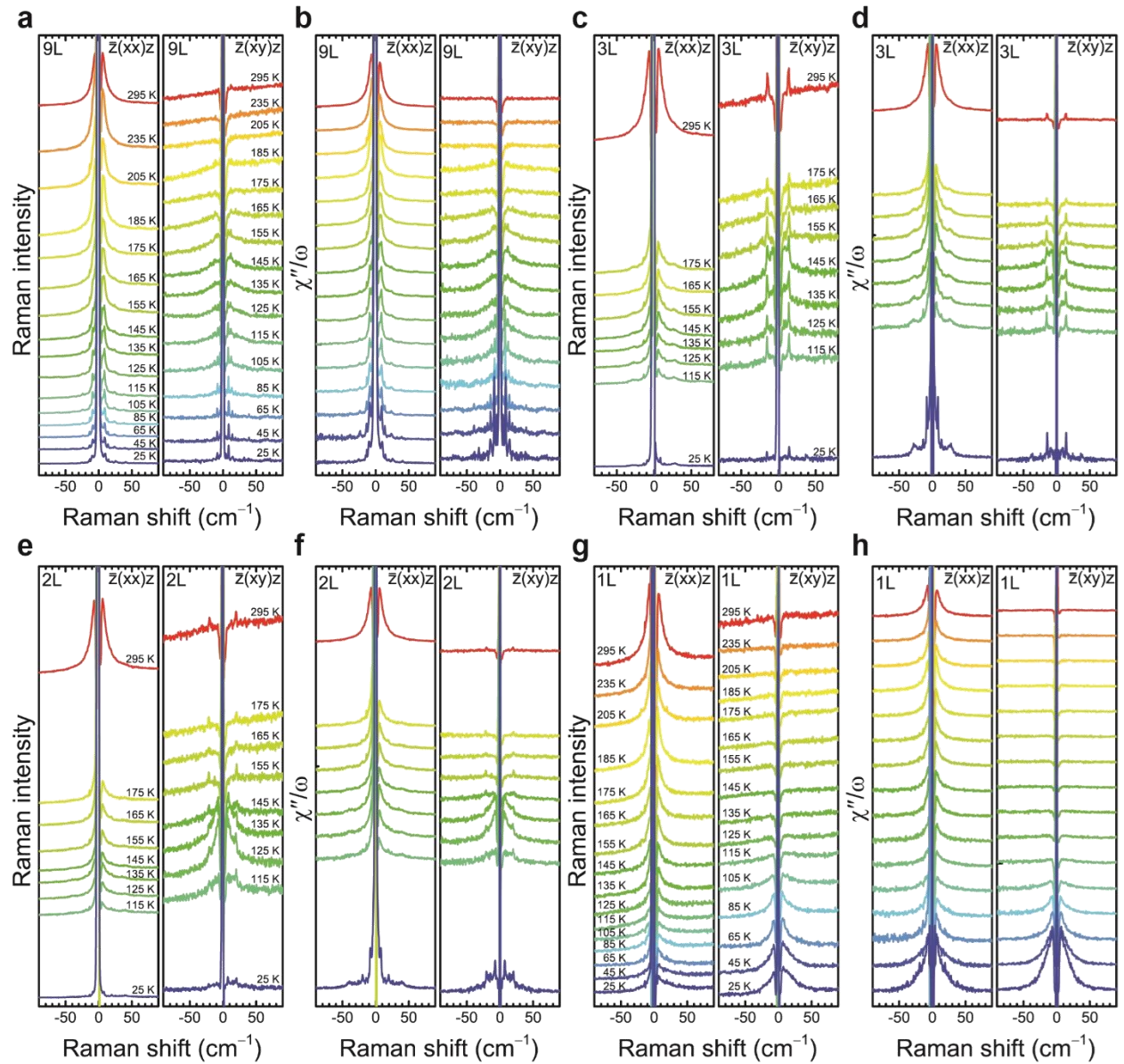
Supplementary Figure 12 | Extracting transition temperature by using ΔP_2 . a,b, Temperature dependence of ΔP_2 for various thicknesses for $\text{NiPS}_3/\text{SiO}_2/\text{Si}$ samples (a), and $\text{NiPS}_3/\text{hBN}/\text{SiO}_2/\text{Si}$ samples (b). The curves are fitting to Supplementary Eq. (5), and the error bars indicate experimental uncertainties.



Supplementary Figure 13 | Comparison of substrate effects. **a**, Optical image of NiPS₃ exfoliated on hBN flake on SiO₂/Si. **b,c**, Polarized Raman spectra of NiPS₃ on SiO₂ and NiPS₃ on hBN at $T=295$ K (**b**) and $T=25$ K (**c**). No discernible differences are observed between two substrates.



Supplementary Figure 14 | ΔP_2 in NiPS₃ on hexagonal boron nitride (hBN). a-d, Temperature dependent polarized Raman spectra of bulk (a), 3L (b), 2L (c), 1L (d) NiPS₃ on hBN. e, Temperature dependence of ΔP_2 for various thicknesses. The Error bars indicate experimental uncertainties. Dashed vertical lines show the Néel temperature for each thickness in e.



Supplementary Figure 15 | Temperature dependence of quasi-elastic scattering signals. Low-frequency Raman spectra (**a**, **c**, **e**, **g**) and Bose-Einstein-factor-corrected Raman response $\chi''(\omega)/\omega$ (**b**, **d**, **f**, **h**) for parallel- and cross-polarization configurations from 9L to 1L NiPS₃.

● **Supplementary Note 4.**

Monte Carlo simulations

We performed Monte Carlo simulations to calculate the physical quantities in N_z layers of stacked honeycomb lattice of spins. Each layer contains $N \times N$ honeycombs. The spin system is described by the Hamiltonian:

$$\begin{aligned}
 H = & J_1 \sum_{\langle i,j \rangle} [S_i^x S_j^x + S_i^y S_j^y + \alpha S_i^z S_j^z] + J_2 \sum_{\langle\langle i,k \rangle\rangle} [S_i^x S_k^x + S_i^y S_k^y + \alpha S_i^z S_k^z] \\
 & + J_3 \sum_{\langle\langle\langle i,l \rangle\rangle\rangle} [S_i^x S_l^x + S_i^y S_l^y + \alpha S_i^z S_l^z] + J' \sum_{[i,m]} [S_i^x S_m^x + S_i^y S_m^y + \alpha S_i^z S_m^z],
 \end{aligned} \tag{6}$$

where single, double, and triple angular brackets in the sums denote nearest, next-nearest, third-nearest neighbors on the same plane, respectively, while square brackets denote nearest neighbors along the stacking direction.

We have performed Monte Carlo simulations to examine thermodynamic properties for three-dimensional stacked honeycomb lattice by using $N = N_z$. We have computed zigzag magnetization m_z defined by

$$m_z = \frac{1}{2N^2 N_z} \left| \sum_i (-1)^{C_i} \mathbf{S}_i \right|, \tag{7}$$

where C_i is the index of the chain to which the spin \mathbf{S}_i belongs. We also calculate zero-field magnetic susceptibility χ ,

$$\chi \equiv \sum_{\alpha=x,y,z} \left. \frac{\partial m_\alpha}{\partial H_\alpha} \right|_{H \rightarrow 0^+}, \tag{8}$$

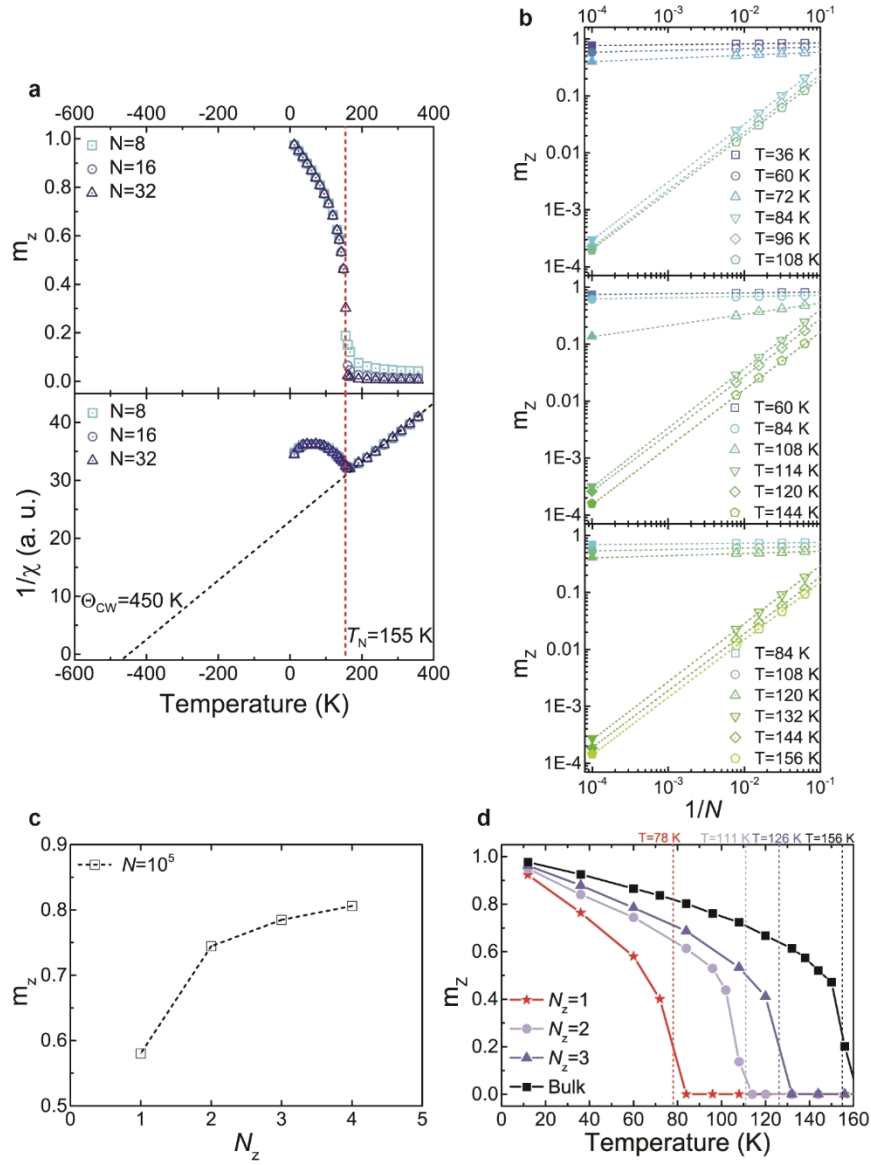
with magnetic field \mathbf{H} and magnetization

$$m \equiv \frac{1}{2N^2 N_z} \sum_i \langle \mathbf{S}_i \rangle. \tag{9}$$

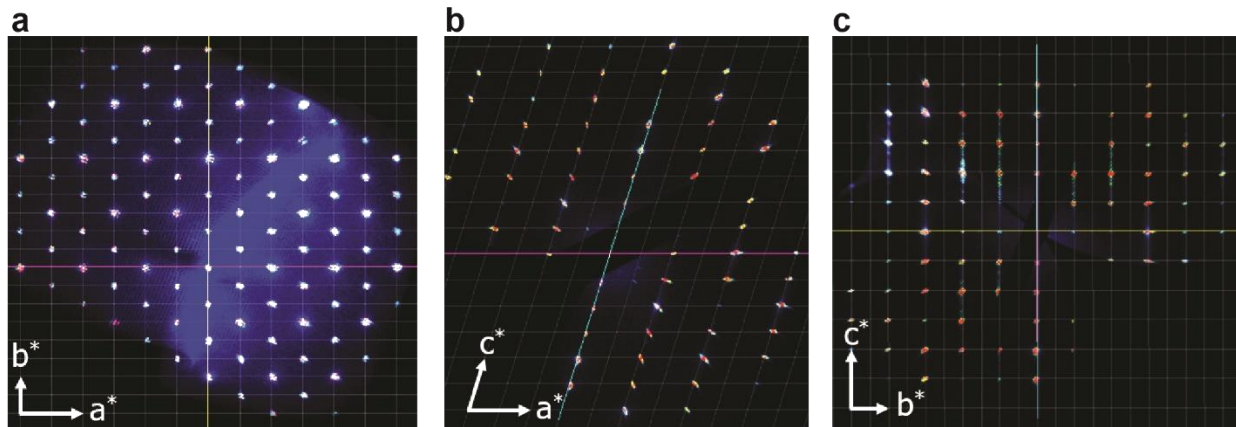
We have used parameters $J_1 S(S+1) = 10.3 \text{ meV}$, $J_2 = J_3 = J_1$, $J' = -J_1$, $\alpha = 0.66$; the inter-layer coupling is included for the bulk and the few-layer computations, and the intra-layer couplings are simplified due to computational costs, which do not affect qualitatively the Monte

Carlo results. Under these parameters the spin system undergoes the phase transition into a magnetically ordered state with zigzag magnetic order at $T_N \approx 155$ K .

With these exchange couplings we examined the properties of few layers of honeycomb lattice through Monte Carlo simulations. The simulations have been performed up to the size $N = 128$ for $N_z = 1, 2, 3, 4$. In Supplementary Fig. 16b, we plot zigzag magnetization at $T = 60$ K as a function of N . The linear behavior in the log-log plot demonstrates well the power-law decrease with N and the resulting powers are close to two at high temperatures. As the temperature decreases the power decreases below a certain temperature, and approaches zero. By using the best linear fit, we have obtained zigzag magnetization m_z for $N = 10000$, which corresponds to typical sizes of samples in experiments. The plot of m_z versus N_z in Supplementary Fig. 16c demonstrates well that the zigzag magnetization for $N_z = 1$ is reduced in large systems much lower in comparison with $N_z > 1$. In Supplementary Fig. 16d we also plot the temperature dependence of extrapolated m_z for $N_z = 1, 2, 3$ together with that of three-dimensional systems. We observe that the onset temperature of m_z decreases monotonically with the decrease of N_z , which exhibits qualitative agreement with the experimental results in few layers of NiPS₃.



Supplementary Figure 16 | Monte Carlo simulation results. **a**, Zigzag magnetization m_z and inverse magnetic susceptibility $1/\chi$ as a function of temperature T in a three-dimensional stacked honeycomb lattice. The onset of zigzag magnetization (red line) occurs at $T_N = 155$ K and the extrapolation of high-temperature part of inverse magnetic susceptibility (green line) gives Curie temperature $\Theta_{CW} = 450$ K. **b**, Log-log plot of zigzag magnetization m_z for $N_z = 1$ (top), 2 (middle), 3 (bottom) layers of honeycomb lattice as a function of lattice N at various temperatures T . Lines are best linear fits of the zigzag magnetization for each N_z and T . Filled symbols are extrapolated values at $N = 10000$. **c**, Zigzag magnetization m_z extrapolated to typical size $N = 10000$ as a function of the number of layers N_z at $T = 60$ K. **d**, Zigzag magnetization extrapolated to $N = 10000$ as a function of temperature T for $N_z = 1, 2, 3$ layers and three-dimensional bulk lattice.



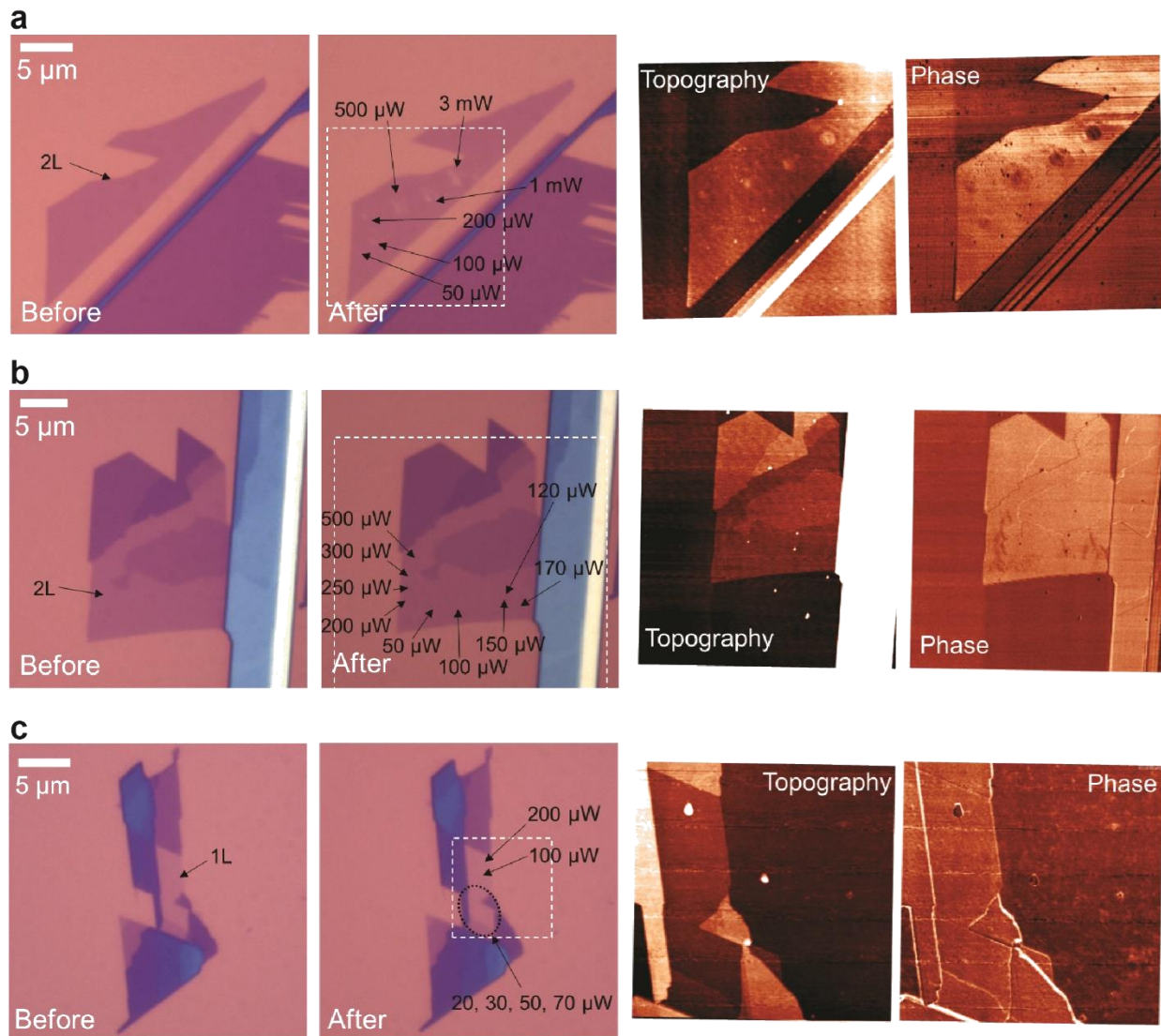
Supplementary Figure 17 | X-ray diffraction patterns of NiPS₃ single crystal. a-c, Bragg peaks of bulk NiPS₃ mapped on the reciprocal lattice for *ab* (a), *ac* (b), and *bc* (c) planes.

● Supplementary Note 5.

Degradation test for few-layer NiPS₃

Exfoliated few-layer NiPS₃ samples are relatively stable but show photo-degradation when the sample are exposed to focused laser in ambient conditions. To check that the few-layer samples are stable under the experimental conditions, we performed the degradation test of few-layer NiPS₃ samples as follow.

First, we checked photo-degradation of NiPS₃ in ambient air. We exposed a 2L NiPS₃ sample to focused laser beams with several different powers in ambient air for 1 min and obtained optical and atomic force microscopy (AFM) images (see Supplementary Fig. 18a). Some photo-degradation was observed on sample surfaces exposed to the laser. The degradations are more readily observed in the phase contrast image of AFM. Some degradation is observed from a spot exposed to as low-power as a 50- μ W laser beam. Next, we performed similar tests for 1L and 2L NiPS₃ samples in vacuum (see Supplementary Figs. 18b and c). The samples were exposed to focused laser beams with several different powers for more than 30 min. There is no discernible change in the optical images. In AFM images, minor degradations can be observed from spots if the power of laser is higher than 150 μ W. Since the power of the laser we used in our experiment was 100 μ W, we can assume that photo-degradation should be minimal.



Supplementary Figure 18 | Photo-degradation test for few-layer NiPS₃. Optical images before and after exposing to several laser powers and atomic force microscopy images of topography and phase after exposing to laser of 2L NiPS₃ in ambient air (a), and 2L (b) and 1L NiPS₃ in vacuum (c).

Supplementary References.

1. Zhao, Y. *et al.* Interlayer Breathing and Shear Modes in Few-Trilayer MoS₂ and WSe₂. *Nano Lett.* **13**, 1007–1015 (2013).
2. Zhang, X. *et al.* Raman spectroscopy of shear and layer breathing modes in multilayer MoS₂. *Phys. Rev. B* **87**, 115413 (2013).
3. Brec, R. Review on structural and chemical properties of transition metal phosphorous trisulfides MPS₃. *Solid State Ionics* **22**, 3–30 (1986).
4. Wildes, A. R. *et al.* Magnetic structure of the quasi-two-dimensional antiferromagnet NiPS₃. *Phys. Rev. B* **92**, 224408 (2015).
5. Fouet, J. B., Sindzingre, P. & Lhuillier, C. An investigation of the quantum J₁-J₂-J₃ model on the honeycomb lattice. *Eur. Phys. J. B* **20**, 241–254 (2001).
6. Mulder, A., Ganesh, R., Capriotti, L. & Paramekanti, A. Spiral order by disorder and lattice nematic order in a frustrated Heisenberg antiferromagnet on the honeycomb lattice. *Phys. Rev. B* **81**, 214419 (2010).
7. Bishop, R. F., Li, P. H. Y., Farnell, D. J. J. & Campbell, C. E. The frustrated Heisenberg antiferromagnet on the honeycomb lattice: J₁-J₂ model. *J. Phys. Condens. Matter* **24**, 236002 (2012).
8. Li, P. H. Y., Bishop, R. F. & Campbell, C. E. Phase diagram of a frustrated spin-1/2 J₁-J₂ XXZ model on the honeycomb lattice. *Phys. Rev. B* **89**, 220408 (2014).
9. Ressouche, E. *et al.* Magnetoelectric MnPS₃ as a candidate for ferrotoroidicity. *Phys. Rev. B* **82**, 100408 (2010).
10. Lançon, D. *et al.* Magnetic structure and magnon dynamics of the quasi-two-dimensional antiferromagnet FePS₃. *Phys. Rev. B* **94**, 214407 (2016).
11. Nguyen, T. M. H. *et al.* Two-magnon scattering in the 5d all-in-all-out pyrochlore magnet Cd₂Os₂O₇. *Nat. Commun.* **8**, 251 (2017).
12. Toth, S. & Lake, B. Linear spin wave theory for single-Q incommensurate magnetic structures. *J. Phys. Condens. Matter* **27**, 166002 (2015).
13. del Corro, E. *et al.* Atypical Exciton–Phonon Interactions in WS₂ and WSe₂ Monolayers Revealed by Resonance Raman Spectroscopy. *Nano Lett.* **16**, 2363–2368 (2016).
14. Carvalho, B. R. *et al.* Intervalley scattering by acoustic phonons in two-dimensional MoS₂ revealed by double-resonance Raman spectroscopy. *Nat. Commun.* **8**, 14670 (2017).
15. Bernasconi, M. *et al.* Lattice dynamics of layered MPX₃ (M=Mn,Fe,Ni,Zn; X=S,Se) compounds. *Phys. Rev. B* **38**, 12089–12099 (1988).

16. Baltensperger, W. & Helman, J. S. Influence of magnetic order in insulators on the optical phonon frequency. *Helv. Phys. Acta* **41**, 668–673 (1968).
17. Callen, E. Optical Absorption Edge of Magnetic Semiconductors. *Phys. Rev. Lett.* **20**, 1045–1048 (1968).
18. Ashcroft, N. W. & Mermin, N. D. *Solid State Physics*. (Brooks/Cole, 1976).